Chemical Science

ROYAL SOCIETY OF CHEMISTRY

EDGE ARTICLE

View Article Online
View Journal | View Issue

Cite this: *Chem. Sci.*, 2022, **13**, 10461

All publication charges for this article have been paid for by the Royal Society of Chemistry

Received 25th May 2022
Accepted 12th August 2022

DOI: 10.1039/d2sc02915d

rsc.li/chemical-science

Phase-engineered high-entropy metastable FCC $Cu_{2-y}Ag_y(In_xSn_{1-x})Se_2S$ nanomaterials with high thermoelectric performance†

Wanjia Zhang,‡[a] Yue Lou,‡*[a] Hongliang Dong,[b] Fanshi Wu,[a] Janak Tiwari,[c] Zhan Shi,[d] Tianli Feng,[c] Sokrates T. Pantelides[e] and Biao Xu*[a]

Crystal-phase engineering to create metastable polymorphs is an effective and powerful way to modulate the physicochemical properties and functions of semiconductor materials, but it has been rarely explored in thermoelectrics due to concerns over thermal stability. Herein, we develop a combined colloidal synthesis and sintering route to prepare nanostructured solids through ligand retention. Nano-scale control over the unconventional cubic-phase is realized in a high-entropy $Cu_{2-y}Ag_y(In_xSn_{1-x})Se_2S$ ($x = 0$–0.25, $y = 0$, 0.07, 0.13) system by surface-ligand protection and size-driven phase stabilization. Different from the common monoclinic phase, the unconventional cubic-phase samples can optimize electrical and thermal properties through phase and entropy design. A high power factor (0.44 mW m^{-1} K^{-2}), an ultralow thermal conductivity (0.25 W m^{-1} K^{-1}) and a ZT value of 1.52 are achieved at 873 K for the cubic $Cu_{1.87}Ag_{0.13}(In_{0.06}Sn_{0.94})Se_2S$ nanostructured sample. This study highlights a new method for the synthesis of metastable phase high-entropy materials and gives insights into stabilizing the metastable phase through ligand retention in other research communities.

1. Introduction

Thermoelectric devices can directly convert waste heat into electrical power without hazardous emissions and moving parts and have become an attractive option for improving energy utilization in applications such as medical devices,[1] thermal management,[2] cooling[3,4] and thermocells.[5] In general, the energy conversion efficiency of a thermoelectric material is determined by the figure of merit, $ZT = S^2\sigma T/k_{tot}$, where S is the Seebeck coefficient, σ is the electrical conductivity, k_{tot} is the total thermal conductivity, and T is the working temperature. In the past few decades, several strategies such as band convergence,[6–9] resonance level,[10,11] introducing defects,[12,13] and controlling grain size[14,15] have been successfully developed to increase ZT. So far, TE materials have been thoroughly investigated, including SnSe,[16] GeTe,[17] carbon hybrids,[18] Cu_2Se[19] and organic thermoelectrics.[20] However, strong coupling between S, σ, and k_{tot} remains a formidable challenge for further optimization of thermoelectric performance.

Phase engineering focuses on the synthesis of unconventional phases, phase transformations and phase-based heterostructures. In particular, preparation of unconventional phases in nanomaterials through carefully regulating reaction kinetics and/or thermodynamics endows them with distinctive properties.[21–24] Meanwhile, this concept may also be developed in a coordinated way with other aspects, including composition, architecture, and dimensionality engineering, to realize a higher level of control over thermoelectric materials. Recently, high-entropy alloys (HEAs), in which multiple elements are utilized to occupy equivalent atomic sites resulting in increased configurational entropy, have provided a new means for improving the thermoelectric performance of materials.[25–27] Based on the core effects of HEAs, a synergy of band structure engineering and all-scale hierarchical microstructures is well realized.[28–30] However, the metastable-phase engineering of

[a]*Department of Chemistry and Chemical Engineering, Nanjing University of Science and Technology, Nanjing, Jiangsu 210094, P. R. China. E-mail: louyue@njust.edu.cn; xubiao@njust.edu.cn*

[b]*Center for High Pressure Science and Technology Advanced Research, Shanghai 201203, China*

[c]*Department of Mechanical Engineering, The University of Utah, Salt Lake City, UT 84112, USA*

[d]*State Key Laboratory of Inorganic Synthesis and Preparative Chemistry, College of Chemistry, Jilin University, Changchun 130012, P. R. China*

[e]*Department of Physics and Astronomy and Department of Electrical and Computer Engineering, Vanderbilt University, Nashville, TN 37235, USA*

† Electronic supplementary information (ESI) available: List of chemicals, preparation of Cu_2SnSe_3, Cu_2SnSe_2S, $Cu_2In_xSn_{1-x}Se_2S$, $Cu_3InSnSe_3S_2$ and $Cu_{2-y}Ag_y(In_{0.06}Sn_{0.94})Se_2S$ nanocrystals, spark plasma sintering, characterization, measurement of thermoelectric properties, DFT calculation, formation energy calculation, the calculation details of the Lorentz factor (L) and density of states effective mass (m_d*) *via* the single parabolic band (SPB) model, the calculation details of heat capacity C_p *via* the Debye-3 Einstein model, crystal structure characterization, microstructure and composition, electronic and phononic band structures and thermoelectric properties. See https://doi.org/10.1039/d2sc02915d

‡ These two authors contributed equally.

high-entropy bulk thermoelectric materials remains a great challenge. According to the Gibbs free energy equation ($G = H - TS$, where T is temperature, S is entropy, and H is enthalpy), high mixing entropy at high temperature can effectively reduce the G of the alloy system and promote the formation of the solid solution phase of the alloy. Therefore, the traditional synthesis of high-entropy alloys mostly relies on the high temperature melting method, and metastable phases in high-entropy systems are hard to achieve.[26] In contrast, phase engineering of nanomaterials may avoid high temperatures and pressures, because the molar Gibbs energy, the molar entropy and the molar enthalpy increase as the particle size decreases.[31–33] In colloidal synthesis, the retained surface ligand can prevent grain growth and stabilize metastable phases through tuning the surface-related H. On the basis of this, phase engineering of high entropy nanomaterials can be well realized by changing the reaction conditions such as the stoichiometric ratio of precursor to surfactant, and sintering conditions. Therefore, developing ligand-retention synthetic strategies for preparation of high-entropy nanostructured solids is of great importance but still remains unexplored.

Cu_2SnSe_3 is a p-type semiconductor with a direct bandgap of 0.84 eV, which has attracted increasing attention in the thermoelectric community due to its compositionally tunable electronic structure and intrinsically low lattice thermal conductivity.[34,35] Previous studies have shown that the thermoelectric properties of Cu_2SnSe_3 can be improved by modulation doping, synergistic alloying and nanostructuring with second phases.[34–38] For example, Li *et al.*[34] showed that (Ag, In)-co-doping provides an effective solution to optimize the ZT of Cu_2SnSe_3 to 1.42 at 823 K. Ming *et al.*[35] achieved a record high ZT of 1.51 at 858 K for $Cu_2Sn_{0.82}In_{0.18}Se_{2.7}S_{0.3}$ *via* alloying S and doping In. However, the structures of these materials are mostly monoclinic, while the cubic structure with high symmetry as a metastable phase is rarely obtained, as it requires thermodynamic control through specific synthetic conditions.

In this work, as shown in Scheme 1, we firstly adopt colloidal synthesis, performed at a low temperature for short reaction times, to obtain metastable wurtzite $Cu_{2-y}Ag_y(In_xSn_{1-x})Se_2S$ nanocrystals. Different from the monoclinic bulk materials in most of the literature,[34–36,39–42] a series of multinary chalcogenide nanostructured solids with a metastable cubic phase are obtained after spark plasma sintering (SPS). Here, oleylamine (OAm) and dodecanethiol (DDT) coated on nanoparticle surfaces could carbonize to protective amorphous carbon shells that can restrict the growth of nanoparticles and stabilize a metastable cubic phase of nanostructured solids. As a result, the cubic-phase, high-entropy $Cu_{1.87}Ag_{0.13}(In_{0.06}Sn_{0.94})Se_2S$ nanomaterial achieves a high power factor (PF) of 0.44 mW m^{-1} K^{-2}, an ultralow thermal conductivity of 0.25 W m^{-1} K^{-1}, and a peak ZT of 1.52 at 873 K.

2. Results and discussion

2.1 Phase engineering through surface-ligand protection

Cu_2SnSe_3, Cu_2SnSe_2S, $Cu_2In_xSn_{1-x}Se_2S$ (x = 0.05–0.4), $Cu_3InSnSe_3S_2$, and $Cu_{2-y}Ag_y(In_{0.06}Sn_{0.94})Se_2S$ (y = 0, 0.07, 0.13) nanocrystals were synthesized by the reaction of metal chlorides and diphenyl diselenide/DDT/OAm solution as the precursors (see the Experimental section in the ESI† for details). X-ray diffraction (XRD) patterns (Fig. S1a†) suggest that the as-synthesized nanocrystals have a wurtzite structure derived from ZnSe, in which the cationic Zn^{2+} ions are substituted by Cu^+, In^{3+}, and Sn^{4+}, and anionic Se^{2-} ions are partly substituted

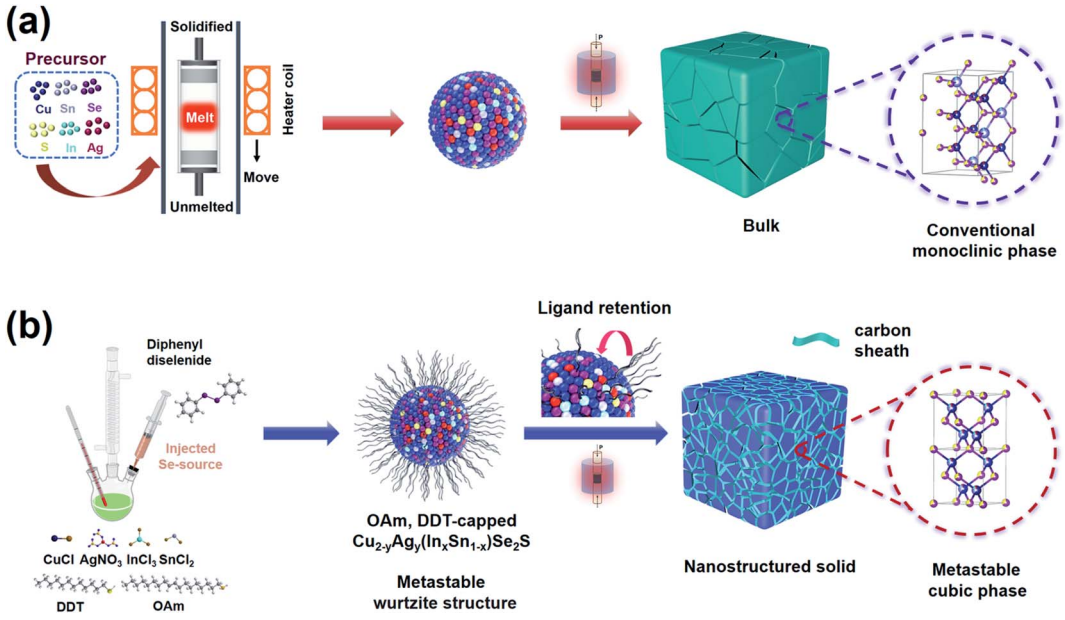

Scheme 1 (a) The monoclinic Cu_2SnSe_3-based bulk materials reported in most of the literature[34–36,39–42] are obtained *via* the high temperature melting method. (b) Synthetic methods of the metastable wurtzite structure $Cu_{2-y}Ag_y(In_xSn_{1-x})Se_2S$ nanocrystals and metastable cubic $Cu_{2-y}Ag_y(In_xSn_{1-x})Se_2S$ nanostructured solids.

by S^{2-}.[43] As a representative, the powder XRD pattern of $Cu_3InSnSe_3S_2$ nanocrystals was analyzed by the Rietveld refinement method (Fig. S1b†), in which the crystal structure fitted well to the wurtzite structure with space group $P6_3mc$ (186) and the lattice parameters are listed in Table S1.† When Ag element is alloyed in $Cu_{2-y}Ag_y(In_{0.06}Sn_{0.94})Se_2S$ ($y = 0.07$ and 0.13), a small fraction of the second phase, CuAgS, is observed in the samples (Fig. S1a†). To characterize the thermoelectric properties of the dense materials compacted from these nanoparticles, the purified nanocrystals were sintered by SPS and characterized by XRD, as shown in Fig. 1a. The main peaks of SPSed-Cu_2SnSe_3 match well with the cubic phase Cu_2SnSe_3 (PDF# 65-4145). The peaks shift to high angle after alloying S into the anionic site and/or doping In into the cationic site, indicating the shrinkage of lattice parameters. Interestingly, when the amount of indium increases to a certain amount, SPSed-$Cu_2In_{0.4}Sn_{0.6}Se_2S$ and SPSed-$Cu_3InSnSe_3S_2$ nanostructured solids have a tetragonal structure (space group $I\bar{4}2m$) without impurities, and this tetragonal unit cell can be approximately depicted as a $1 \times 1 \times 2$ supercell of cubic Cu_2SnSe_3 (Fig. 1a and Table S1†). After Ag alloying, SPSed-$Cu_{1.93}Ag_{0.07}(In_{0.06}Sn_{0.94})Se_2S$ shows a cubic structure (Fig. 1c). Due to the larger ionic radius of Ag^+ (1.26 Å) compared to that of Cu^+ (0.96 Å), the diffraction peaks shift toward the low-angle direction with respect to cubic SPSed-$Cu_2In_{0.06}Sn_{0.94}Se_2S$ (Fig. 1a) due to an expansion of the lattice. The cubic $Cu_{1.8}Se$ phase still exists as a second phase in samples and disappears upon increasing In content and/or alloying Ag. In addition, according to the classical theory of grain growth,[44] the Zener pinning effect caused by the introduction of a second phase could inhibit grain growth to some extent.

From a synthetic perspective, a high-entropy system, $Cu_{2-y}Ag_y(In_xSn_{1-x})Se_2S$ ($x = 0$–0.25, $y = 0$, 0.07, 0.13), with two metastable phases (wurtzite nanocrystals and cubic nanostructured solids) is obtained, which is hard to realize in their bulk counterparts. Formation energies of the cubic and monoclinic-phase Cu_2SnSe_3, Cu_2SnSe_2S, $Cu_2In_{0.06}Sn_{0.94}Se_2S$, and $Cu_{1.87}Ag_{0.13}(In_{0.06}Sn_{0.94})Se_2S$, and tetragonal-phase $Cu_3InSnSe_3S_2$ are calculated by density functional theory (DFT). Indeed, all monoclinic crystals show lower formation energy than the metastable cubic phase (Table S2†). The colloidal synthetic strategy for monodisperse multinary chalcogenide nanocrystals and the following SPS process are the key factors for the retention of the metastable phase. As shown in Fig. 1f, FTIR spectrometry was performed to verify the surface ligand of OAm in a solution-synthesized $Cu_{1.87}Ag_{0.13}(In_{0.06}Sn_{0.94})Se_2S$ sample. The presence of the OAm molecule is indicated by the symmetric and asymmetric stretching vibrations of $-NH_2$ at 3430.74 cm^{-1}, the bending vibrations of C=C and $-NH_2$ bonds

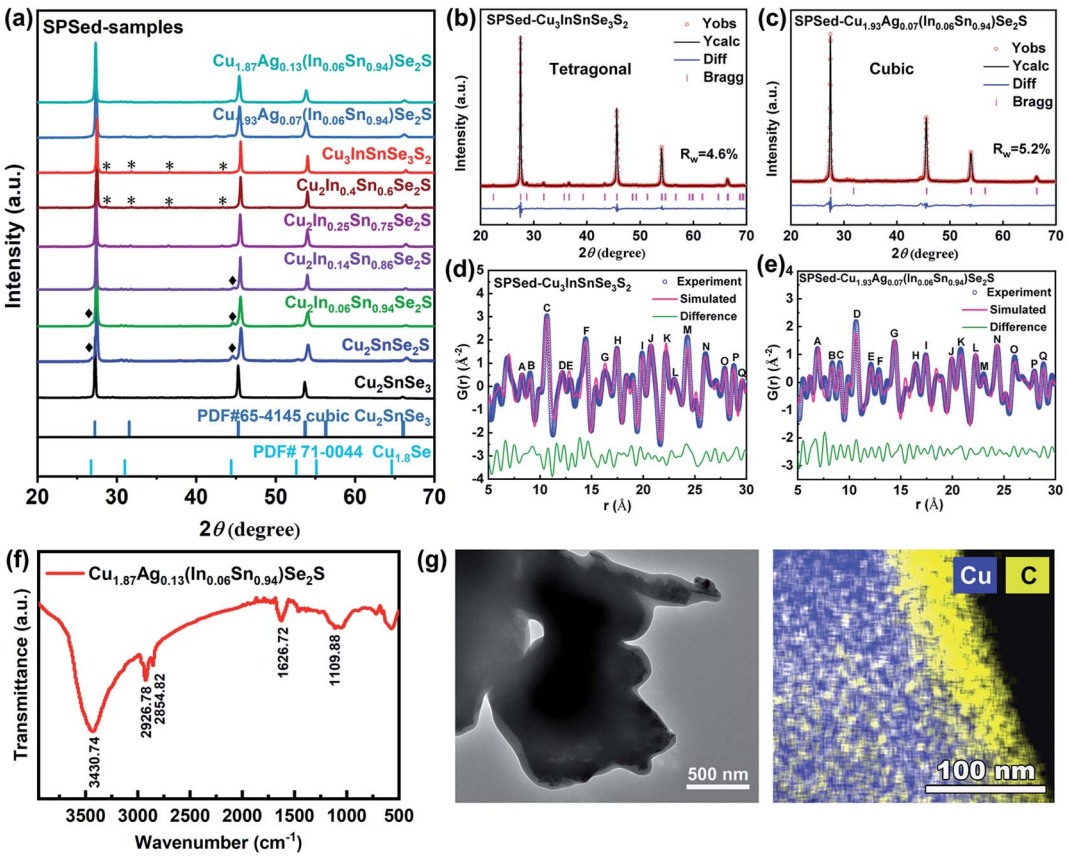

Fig. 1 (a) Powder X-ray diffraction (PXRD) patterns of the SPSed-samples. Rietveld refinement results of (b) SPSed-$Cu_3InSnSe_3S_2$ and (c) SPSed-$Cu_{1.93}Ag_{0.07}(In_{0.06}Sn_{0.94})Se_2S$. PDF fit to the $G(r)$ function in the range of 5–30 Å using the tetragonal model for (d) SPSed-$Cu_3InSnSe_3S_2$ and cubic model for (e) SPSed-$Cu_{1.93}Ag_{0.07}(In_{0.06}Sn_{0.94})Se_2S$. (f) FTIR spectrum of solution-synthesized $Cu_{1.87}Ag_{0.13}(In_{0.06}Sn_{0.94})Se_2S$. (g) TEM image and EDS element map of Cu and C for SPSed-$Cu_{1.87}Ag_{0.13}(In_{0.06}Sn_{0.94})Se_2S$.

at 1626.72 cm^{-1}, and the bending vibration of the C–N bond at 1109.88 cm^{-1}. During the nanocrystal consolidation process, OAm as a surfactant capping agent at the surface of colloidal nanoparticles can decrease the surface free energy of nanocrystals, simultaneously acting as a controllable molecular solder,[45] which might have a dominant effect that restricts the growth of nanoparticles and stabilizes the metastable phase.[46–49] Detailed evidence is shown in SEM and TEM images (Fig. 6b andc, and S9a and b†), and the EDS element map of SPSed-$Cu_{1.87}Ag_{0.13}(In_{0.06}Sn_{0.94})Se_2S$ confirms the existence of carbon after sintering (Fig. 1g). In addition, the contents of hydrogen (0.05 wt%) and carbon (1.15 wt%) were measured in the SPSed-$Cu_{1.87}Ag_{0.13}(In_{0.06}Sn_{0.94})Se_2S$ sample, and the results indicate that some of the surface ligands were converted into a mixture of organic hydrocarbons between nanograins of nanostructured solids during the sintering process (Fig. S9c†). Based on size reduction, metastable cubic nanostructured solids Cu_2SnSe_3 and $Cu_{2-y}Ag_y(In_xSn_{1-x})Se_2S$ ($x = 0$–0.25, $y = 0$, 0.07, 0.13) compacted from the corresponding nanoparticles are obtained, which are different from the conventional monoclinic (space group *Cc*) structure of bulk Cu_2SnSe_3-based materials.[34–36,39–42] In addition, the successful synthesis of Cu_2SnSe_3 and Cu_2SnSe_2S cubic nanostructured solids with low configuration entropy provides strong evidence that the metastable cubic phase does not originate from entropy effects, which is different from the strategy for stabilizing the cubic structure by entropy optimization in previous papers.[25–27]

In order to understand the local and long-range structures of the as-obtained nanostructured solids, an X-ray pair distribution function (X-PDF) analysis was performed. The corresponding Rietveld results are shown in Fig. 1d and e, and S1d and e.† It is evident that the global X-PDF structures of simulated structure models provide good descriptions of all the samples, demonstrating the overall crystallographic structure. The peaks with chemical bonding information in the diagrams labeled by letters can be well assigned to the atomic pair distances of the samples (Table S3†). As shown in Fig. 1e and S1e,† the residual curve (green curve) of the cubic model establishes much smoother characteristics in the large range from 10 Å to 30 Å, demonstrating long-range highly crystalline structures. In contrast, the local bonding interactions (5–10 Å) deviate significantly from the simulated profile for the cubic model, as observed from the asymmetric peaks and large fluctuations in the green line. Such a phenomenon is an indication of the local structural distortion with the unbalanced long and short bond lengths. The coexistence of the high-symmetry long-range structure and distorted local structure could be an example of ideal thermoelectric materials based on the 'phonon-glass, electron-crystal' concept that could lead to high electrical conductivity and low thermal conductivity and finally achieve a high *ZT* value.[50,51]

2.2 Microstructure and composition

The microstructures of the as-synthesized samples were comprehensively characterized. First, the hexagonal (wurtzite) structure of Cu_2SnSe_3 is confirmed with an average size of around 30 (±10) nm by transmission electron microscopy (TEM) (Fig. S3a and b†). Then, thiol is added to the reaction system as the S source and surfactant capping agent, which can passivate the crystalline facets of the wurtzite nanocrystals, and thus realize size control. As a result, the synthesized Cu_2SnSe_2S and $Cu_3InSnSe_3S_2$ nanocrystals show hexagonal structures with an average size of 10 (±2) nm (Fig. S4a and b and S5a†). Elemental mapping measurement was performed to identify the presence of Cu, Ag, In, Sn, Se, and S elements in nanoparticles of Cu_2SnSe_3, Cu_2SnSe_2S, SPSed-Cu_2SnSe_3, SPSed-Cu_2SnSe_2S, and SPSed-$Cu_{1.87}Ag_{0.13}(In_{0.06}Sn_{0.94})Se_2S$. All elements in the samples show homogeneous distributions, and no significant local element enrichment is observed (Fig. S3c, S4c, S6b, S7b and S11d†). For nanostructured solids, Fig. S9a and b† show the scanning electron microscopy (SEM) surface micrographs of SPSed-$Cu_2In_{0.06}Sn_{0.94}Se_2S$ and SPSed-$Cu_{1.87}Ag_{0.13}(In_{0.06}Sn_{0.94})Se_2S$ pellets. A slight grain growth of nanoparticles can be observed during the sintering process and the final average grain sizes are 63.06 (±30) and 131.98 (±50) nm for SPSed-$Cu_2In_{0.06}Sn_{0.94}Se_2S$ and SPSed-$Cu_{1.87}Ag_{0.13}(In_{0.06}Sn_{0.94})Se_2S$, respectively. Fig. S10a and d and S11a† show the high-resolution TEM (HRTEM) images of the SPSed-Cu_2SnSe_3, SPSed-Cu_2SnSe_2S, and SPSed-$Cu_{1.87}Ag_{0.13}(In_{0.06}Sn_{0.94})Se_2S$ samples. The inverse fast Fourier transform (IFFT) images (Fig. S10b and e and S11b†) clearly show the highly dense dislocation arrays. In order to investigate the strain fields from distorted lattices caused by the strong mismatch of the atomic radius, geometric phase analysis (GPA) was performed based on IFFT images to calculate the strains. As shown in Fig. S10c and f and S11c,† strong strain distribution fluctuations can be observed in the SPSed samples, which should strongly affect the thermal transport process.

To further verify the single-phase and high-entropy configuration in the as-synthesized $Cu_3InSnSe_3S_2$ and SPSed-$Cu_3InSnSe_3S_2$, high-angle annular dark-field scanning transmission electron microscopy (HAADF-STEM) was conducted. Fig. 2a and e show the HAADF-STEM images of a $Cu_3InSnSe_3S_2$ nanoparticle and SPSed-$Cu_3InSnSe_3S_2$ nanostructured solid viewed along the [001] and [110] zone axes, respectively. The atomic models of the hexagonal structure and tetragonal structure are in good agreement with the experimental images, indicating the consistency of the atomic lattices and positions of all atoms (Fig. 2b and f). As shown in Fig. 2d, all elements are distributed in the nanoparticle, and Cu and S are a little bit aggregated in the center of the particle. From our results and some literature reports,[52,53] we believe that the copper thiolate in solution could preferentially decompose into a $Cu_{2-x}S$ crystal nucleus due to its higher reactively. Then highly active diphenyl diselenide (PhSeSePh) rapidly decomposes at high temperatures after injection and triggers the growth of nanocrystals, in which Se, Sn and In atoms gradually diffuse into the $Cu_{2-x}S$ crystal nucleus simultaneously with the epitaxial growth and maturation process. Therefore, enrichment of Cu and S elements in the middle of individual nanoparticles can be attributed to the preferential nucleation process of 1-dodecanethiol (both as a ligand and sulfur source) in the precursor solution and Cu before the injection of Se sources. As shown in Fig. 2h and S8,†

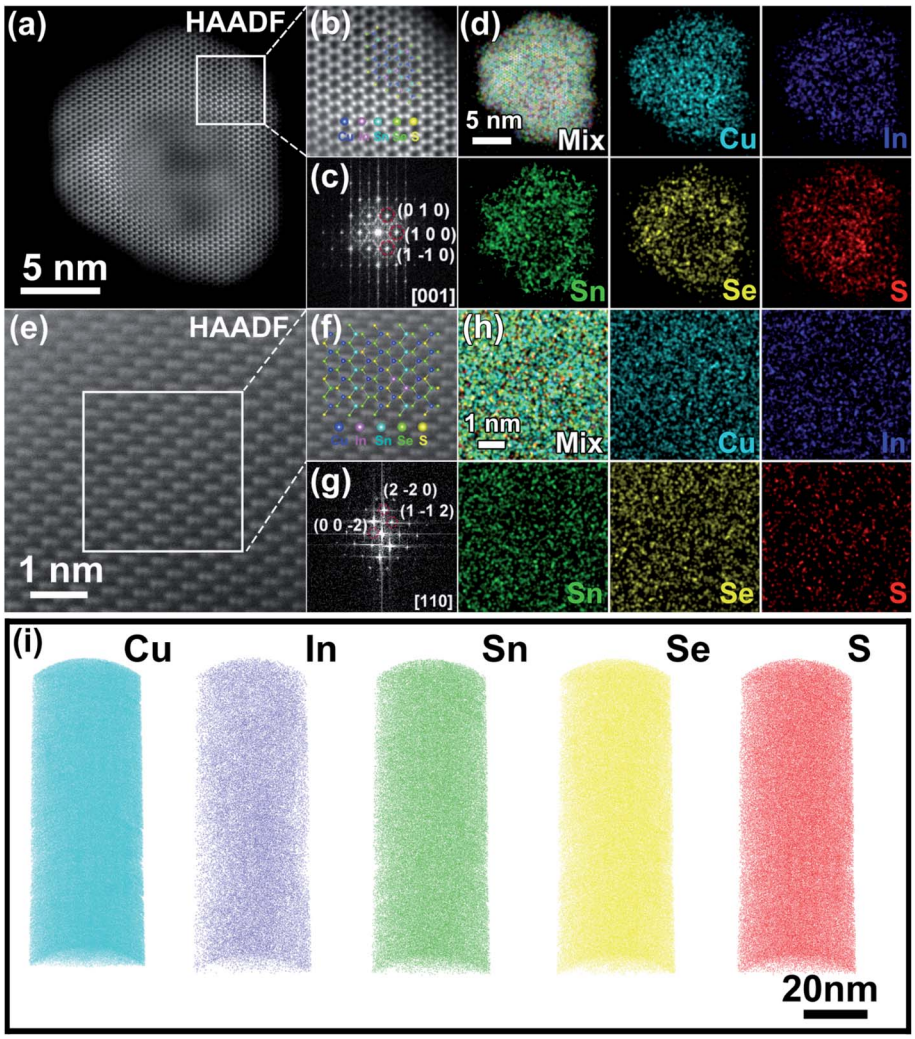

Fig. 2 Atomic structure recognition of solution-synthesized and SPSed-$Cu_3InSnSe_3S_2$. (a) Atomic-resolution HAADF-STEM image, (b) atomic model, (c) corresponding FFT along the [001] zone axis and (d) EDS mapping of the as-synthesized $Cu_3InSnSe_3S_2$ nanoparticle. (e) Atomic-resolution HAADF-STEM image, (f) atomic model, (g) corresponding FFT along the [110] zone axis and (h) EDS mapping of the SPSed-$Cu_3InSnSe_3S_2$ sample. (i) 3D-APT images showing the elemental distribution and multicomponent nature in the SPSed-$Cu_2In_{0.09}Sn_{0.91}Se_2S$.

the EDS mapping of the SPSed-$Cu_3InSnSe_3S_2$ sample demonstrates that the distribution of all elements is homogeneous in the nanostructured solid.

Atom probe tomography (APT) analysis provides the mapping of three-dimensional microstructural and compositional information with sub-nanometer spatial accuracy and elemental sensitivity in the range of tens of ppm,[54] which can provide solid evidence that these elements are indeed homogeneously distributed in the nanostructured solid at the atomic scale. The 3D atomic maps and the nearest-neighbor (NN) atomic distribution of SPSed-$Cu_2In_{0.09}Sn_{0.91}Se_2S$ are shown in Fig. 2i and S14,† respectively. The measured NN atomic distance histograms of each element completely overlap with the calculated curves (Fig. S14†) without deviating from the randomized Gaussian peak, revealing the homogeneous distribution of the Cu, In, Sn, Se, and S elements. The homogeneous and disordered distribution of all the elements on the macroscale, nanoscale, and atomic-scale confirms that the as-synthesized nanostructured solid is a high-entropy multinary metal chalcogenide.

2.3 Electronic and phononic band structures

To gain insight into the evolution of electronic states in the conventional monoclinic structure and metastable cubic structure, DFT calculations were performed. Fig. 3a and b show the electronic band structures of monoclinic and cubic $Cu_{1.87}Ag_{0.13}(In_{0.06}Sn_{0.94})Se_2S$, respectively. Those of Cu_2SnSe_3, Cu_2SnSe_2S, and $Cu_2In_{0.06}Sn_{0.94}Se_2S$ are shown in Fig. S15.† The monoclinic and cubic Cu_2SnSe_3 are direct-band-gap semiconductors with band gaps (E_g) of 0.12 and 0.11 eV, respectively (Fig. S15a and b†). E_g can be effectively enlarged by alloying S into the anionic site of Cu_2SnSe_3 (Fig. S15c and d†). In-Doped Cu_2SnSe_2S pushes the Fermi level (E_f) deep into the multiple bands and turns $Cu_2In_{0.06}Sn_{0.94}Se_2S$ into a highly degenerate

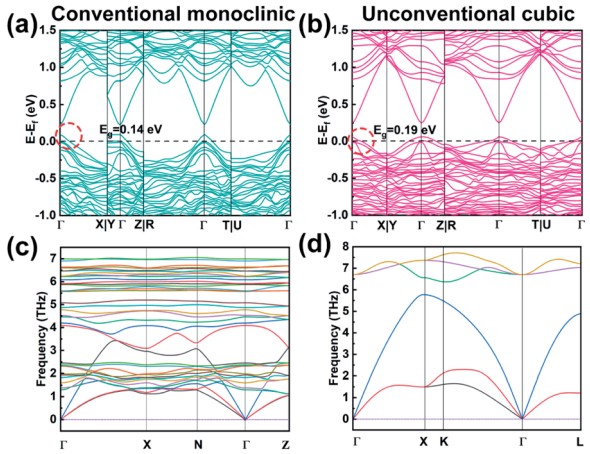

Fig. 3 The electronic energy band structures for (a) monoclinic $Cu_{1.87}Ag_{0.13}(In_{0.06}Sn_{0.94})Se_2S$ and (b) cubic $Cu_{1.87}Ag_{0.13}(In_{0.06}Sn_{0.94})Se_2S$. The phonon dispersions of (c) monoclinic Cu_2SnSe_3 and (d) cubic Cu_2SnSe_3.

semiconductor (Fig. S15e and f†), which thus increases channels for electrical transport. From the valence bands near the Fermi level that are highlighted by the red circles in Fig. 3a and b and S15,† we find that the top three valence bands at the Γ point of the monoclinic structure display band splitting while the cubic structure is degenerate. The cubic phase with high degeneracy can lead to more energy valleys participating in electrical transport.[13]

To gain insight into phonon and thermal properties, we calculated the phonon dispersion relations of monoclinic and cubic Cu_2SnSe_3 based on DFT, as shown in Fig. 3c and d. The monoclinic phase has 12 atoms in a primitive cell and thus 36 phonon branches (Fig. S16a†). The cubic phase has a zinc blende structure, in which Cu and Sn randomly occupy the cation sites with a ratio of 2 : 1, and Se occupies the anion sites (Fig. S16b†). We used the virtual crystal approximation (VCA) to calculate the phonon dispersion of the cubic phase. Under VCA, the cubic phase has a primitive cell that consists of 2 atoms – a virtual atom, made of 2/3 Cu and 1/3 Sn, and a Se atom. The phonon dispersion of the cubic phase does not show any imaginary frequency, indicating that the structure is locally stable. The maximum frequency of the cubic phase is larger than that of the monoclinic phase, indicating that the cubic phase may have stronger bonds. The phonon group velocity, especially for the longitudinal acoustic (LA) branch, of the cubic phase is much larger than that of the monoclinic phase (Fig. S16c†). The volumetric heat capacity of the cubic phase is slightly larger than that of the monoclinic phase (Fig. S16d†), partially because the cubic phase has higher symmetry and packing density. Based on phonon kinetic theory, the lattice thermal conductivity is $k_L = 1/3cv^2\tau$, in which c is the heat capacity, v is the group velocity, and τ is the phonon relaxation time. Since the cubic phase has larger c and v than the monoclinic phase, its τ must be much smaller, in order to have similar or lower k_L. This inference indicates that the disorder and distortion induced by Cu/Sn alloying that was not considered in the VCA in the cubic phase must be strong and induce severe phonon scattering. Additionally, grain boundaries, dislocations, Ag and S alloying and In doping further reduce the phonon relaxation time.

2.4 Thermoelectric properties

2.4.1. Sulfur alloying at the anionic site. Fig. S19† shows the thermoelectric properties of Cu_2SnSe_3 and Cu_2SnSe_2S in the temperature range of 323–873 K. It is found that S-alloying leads to a clear decrease in electrical conductivity (σ) (Fig. S19a†). The positive Seebeck coefficient (S) (Fig. S19b†) indicates that the major charge carrier is holes. The S values of Cu_2SnSe_3 and Cu_2SnSe_2S increase with rising temperature. Specifically, S increases from 28.15 μV K^{-1} for Cu_2SnSe_3 to 133.62 μV K^{-1} for Cu_2SnSe_2S at 323 K by partial replacement of Se with S. Despite the enhanced Seebeck coefficient, the power factor (PF) of Cu_2SnSe_2S (0.37 mW m^{-1} K^{-2} at 873 K) is smaller than that of Cu_2SnSe_3 (0.58 mW m^{-1} K^{-2} at 873 K) (Fig. S19c†) because of the lower electrical conductivity. Cu_2SnSe_2S has a low thermal conductivity (k_{tot}) of 0.43 W m^{-1} K^{-1}, which is about 47% lower than that of non-alloyed Cu_2SnSe_3 (Fig. S19d†), indicating the role of S alloying in reducing k. This result may be caused by the distortion and diminished uniformity of the lattice structure, as well as the coexistence of the minor secondary phase of $Cu_{1.8}Se$, which enhances the scattering of phonons. Since the large decrease in k_{tot} overwhelms the decreased PF, the ZT value of the Cu_2SnSe_2S nanostructured solid is 0.75 at 873 K, higher than that of Cu_2SnSe_3 (Fig. S19e†).

2.4.2. Ag and In alloying at the cationic site. Fig. 4a depicts the temperature dependence of σ of $Cu_{2-y}Ag_y(In_xSn_{1-x})Se_2S$ (x = 0, 0.05, 0.06, 0.25, y = 0, 0.07, 0.13), which show complex dependence on the x and y values. Ag alloying can increase σ from 7.06 × 10^3 S m^{-1} for $Cu_2In_{0.06}Sn_{0.94}Se_2S$ to 9.18 × 10^3 S m^{-1} for $Cu_{1.93}Ag_{0.07}(In_{0.06}Sn_{0.94})Se_2S$ at 873 K. Fig. 4b shows S of $Cu_{2-y}Ag_y(In_xSn_{1-x})Se_2S$ for different values of x and y. S increases with increasing temperature in the range of 323–723 K and then decreases slightly in the high-temperature zone, which may be ascribed to the thermal excitation of minority carriers. Moreover, with an increase in the amount of In, S is boosted from 197 μV K^{-1} for Cu_2SnSe_2S to 298 μV K^{-1} for $Cu_2In_{0.25}Sn_{0.75}Se_2S$ at 873 K. Fig. 4d shows the k_{tot} of $Cu_{2-y}Ag_y(In_xSn_{1-x})Se_2S$. A significant reduction in k_{tot} upon doping In at the Sn site and/or alloying Ag at the Cu site is found, demonstrating the important role of entropy effects.

2.4.3. High crystallographic symmetry leads to high Seebeck coefficient and power factor. In order to understand the electrical transport, effective mass analysis by the Pisarenko plot was done, as shown in Fig. 5a. Compared with the largest $m_d^* = 3.1m_e$ (m_e is the free electron mass) in the monoclinic-phase $Cu_2Sn_{1-y}In_ySe_{2.7}S_{0.3}$ and $Cu_{2-x}Ag_xSn_{1-y}In_ySe_3$ reported by Ming *et al.*[35] and Li *et al.*,[34] the enhancement in symmetry increases the effective mass to $4.0m_e$ in our cubic $Cu_2In_{0.06}Sn_{0.94}Se_2S$ sample, yielding a large Seebeck coefficient. As shown in Fig. 4c, the PF further increases *via* Ag alloying in the whole investigated temperature range. The maximum PF values of 0.45 and 0.44 mW m^{-1} K^{-2} are obtained at 873 K for

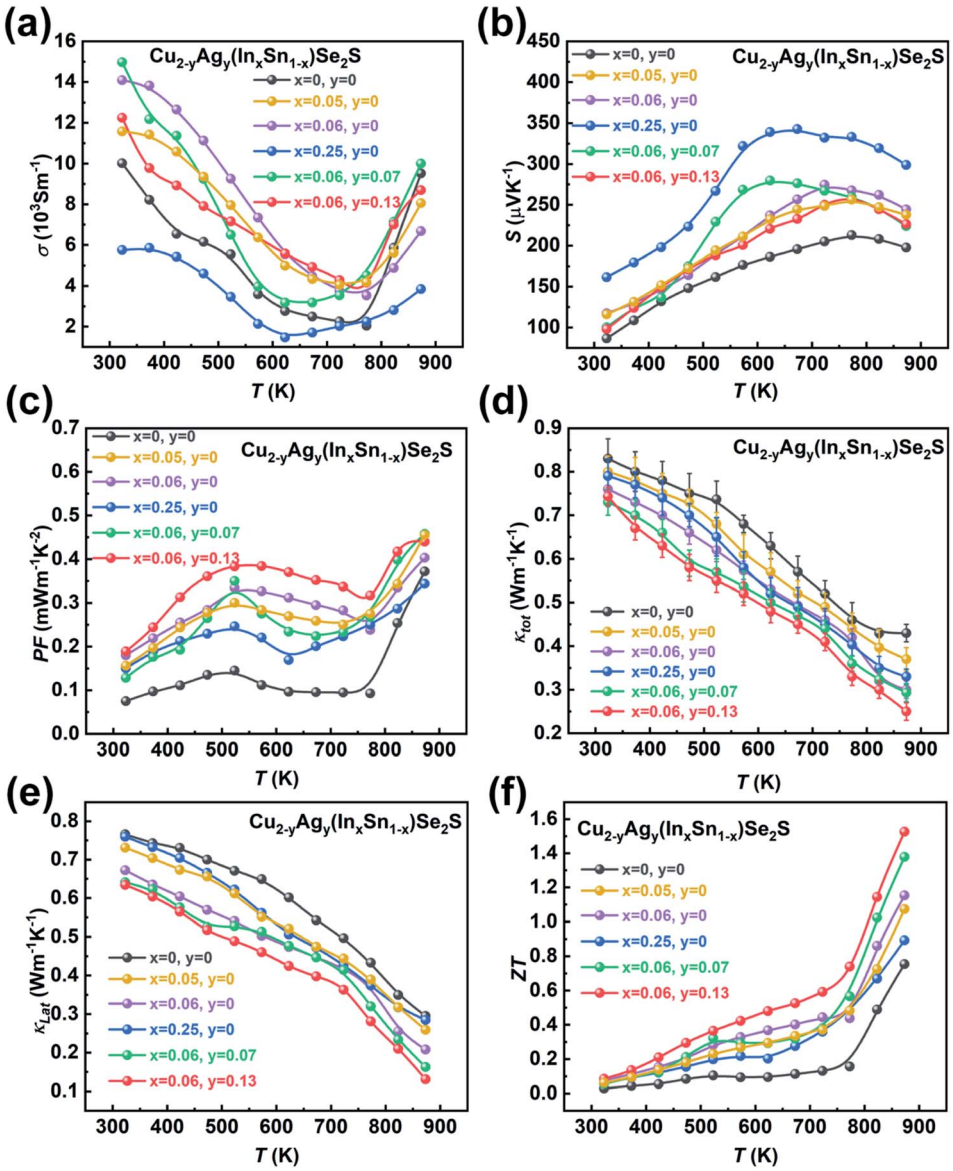

Fig. 4 Temperature dependence of (a) electrical conductivity σ, (b) Seebeck coefficient S, (c) power factor PF, (d) total thermal conductivity k_{tot}, (e) lattice thermal conductivity k_{lat} and (f) ZT values for $Cu_{2-y}Ag_y(In_xSn_{1-x})Se_2S$ ($x = 0, 0.05, 0.06, 0.25$, $y = 0, 0.07, 0.13$).

$Cu_{1.93}Ag_{0.07}(In_{0.06}Sn_{0.94})Se_2S$ and $Cu_{1.87}Ag_{0.13}(In_{0.06}Sn_{0.94})Se_2S$, respectively.

2.4.4. Unique crystal structure and nanostructures lead to ultralow thermal conductivity. The temperature-dependent total (k_{tot}) and lattice (k_{lat}) thermal conductivity for all the samples decline with increasing temperature in the whole investigated temperature range, as exhibited in Fig. 4d and e. The k_{lat} is calculated by $k_{lat} = k_{tot} - k_e$, in which k_e is electronic thermal conductivity and is estimated using the Wiedemann–Franz law, *i.e.*, $k_e = L\sigma T$, where L is the Lorentz factor, calculated based on the single parabolic band (SPB) assumption. The k_{tot} and k_{lat} gradually decrease with In doping, but increase with more In content doping, which should be attributed to the reduction of secondary phase and the decrease of atomic disorder resulting from the transition to the tetragonal phase. Furthermore, the substitution of Ag on the Cu site further decreases the k_{tot} and k_{lat} down to 0.25 and 0.13 W m^{-1} K^{-1} respectively at 873 K for the $Cu_{1.87}Ag_{0.13}(In_{0.06}Sn_{0.94})Se_2S$ sample due to the enhanced scattering of phonons resulting from the distortion and diminished uniformity of the lattice structure, which is comparable to some reported materials with extremely low k, such as $AgSbTe_2$,[55] $Bi_4O_4SeCl_2$ (ref. 56) and TlCuSe.[57] Compared to the thermal conductivity reported in Cu_2SnSe_3-based systems in the literature,[34–36,39] our value is relatively low, as shown in Fig. 5c.

The ultralow k_{lat} of the as-synthesized samples can be attributed to the following three reasons. First, the intrinsic crystal structure of Cu_2SnSe_3-based materials leads to low phonon thermal conductivity. More specifically, the Cu–Se bond constructs a conductive framework for controlling hole

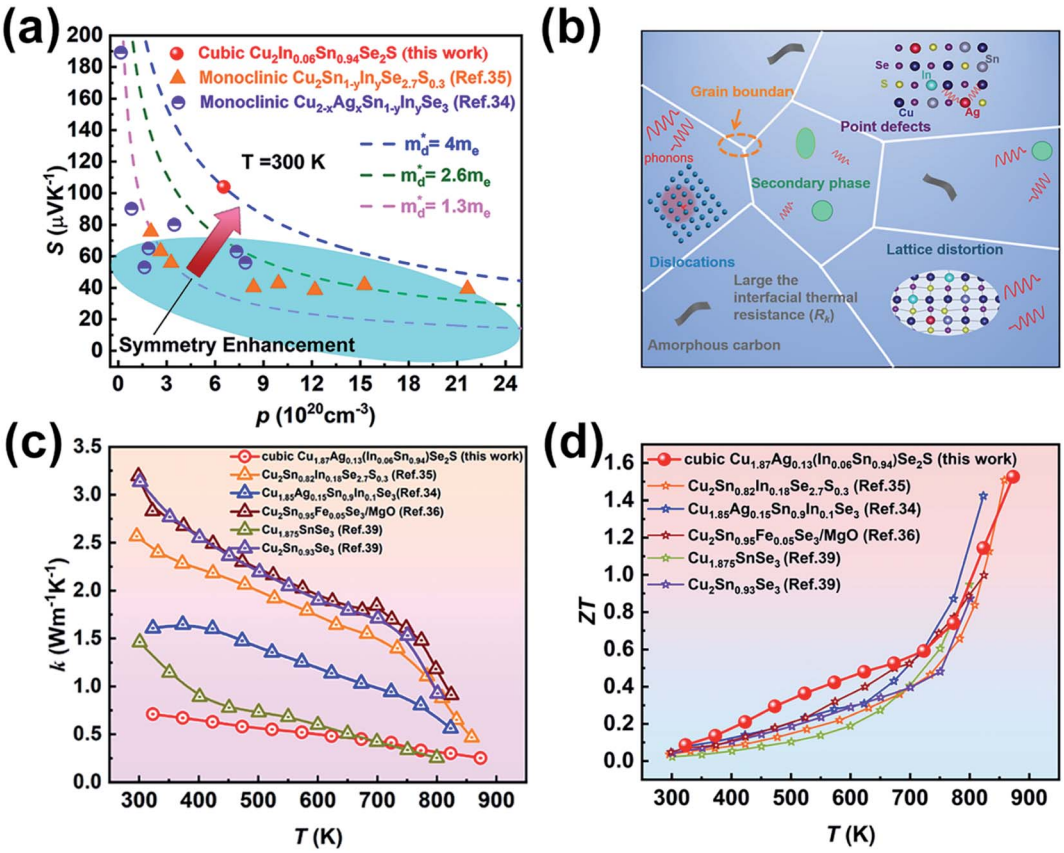

Fig. 5 (a) Variation of Seebeck coefficient S with carrier concentration p for cubic $Cu_2In_{0.06}Sn_{0.94}Se_2S$, in which the blue dotted line is the Pisarenko curve obtained *via* the SPB model. The previously reported data by Ming *et al.*[35] (monoclinic $Cu_2Sn_{1-y}In_ySe_{2.7}S_{0.3}$, $y = 0$–0.21) and Li *et al.*[34] (monoclinic $Cu_{2-x}Ag_xSn_{1-y}In_ySe_3$, $x = 0$–0.15, $y = 0$–0.15) are depicted by orange triangles and purple half-filled circles, respectively. (b) Schematic illustration of the effect of multiscale defects on phonons, including grain boundaries, point defects, lattice distortion, secondary phase, dislocations and amorphous carbon. Comparison of the reported (c) thermal conductivity and (d) ZT values of Cu_2SnSe_3-based materials.[34–36,39]

transport, and cationic doping is allowed to adjust the carrier concentration.[58] Such structural characteristics are similar to those of phonon glass electron crystal (PGEC) compounds,[50,51] which can be confirmed by low-temperature C_p measurement (Fig. S22†). The plot of C_p *vs.* T can be fitted by a Debye model combined with three Einstein modes (black line, the detailed calculation is shown in the ESI†), which illustrates that the contribution to C_p at low temperature is dominated by low-energy optical modes resulting from the weakly bound Cu or Ag-rattlers (Einstein oscillators) that suppress lattice thermal conductivity (k_{lat}).[59–61] Second, the configurational entropy in a material increases through doping and alloying (Fig. S23†). Based on the Boltzmann hypothesis, the configurational entropy (ΔS) is given by:[27]

$$\Delta S = k_B \ln \Omega = -N_A k_B \sum_{i=1}^{n} x_i \ln x_i \quad (1)$$

where k_B is the Boltzmann constant, Ω is the atomic occupation probability, n is the number of substituted components, x_i is the mole content of the ith component, and N_A is Avogadro's number. Among the various components, the possibility of each element having the same lattice size and different atomic size and electronegativity results in lattice distortion,[62] which can be confirmed by the PDF result in Fig. 1e. Short-range disordered structure of multi-component high-entropy materials caused by severe lattice distortion can strongly scatter heat-carrying phonons, reducing the material's lattice thermal conductivity down to its theoretical minimum value. Third, the nano-sized grain effects (boundary scattering) and multidimensional defects (*i.e.*, minor secondary phase of $Cu_{1.8}Se$, point defects, dislocations, and strain fields) (Fig. 5b) induce severe phonon scattering and efficiently reduce the lattice thermal conductivity. Additionally, the amorphous carbon formed by carbonization of ligands after SPS could result in the reduction of thermal conductivity k due to the large interfacial thermal resistance (R_k) resulting from the high dissimilarity in density, sound velocity, and phonon density of states between carbon and the semiconductor matrix.[63,64]

Fig. 4f shows the temperature dependence of ZT values for $Cu_{2-y}Ag_y(In_xSn_{1-x})Se_2S$. Owing to the high PF and low thermal conductivity, $Cu_{1.87}Ag_{0.13}(In_{0.06}Sn_{0.94})Se_2S$ shows the maximum ZT of 1.52 at 873 K. Compared to the ZT values reported in Cu_2SnSe_3-based systems in the literature,[34–36,39] our value is essentially record-high, as shown in Fig. 5d. Compared with the

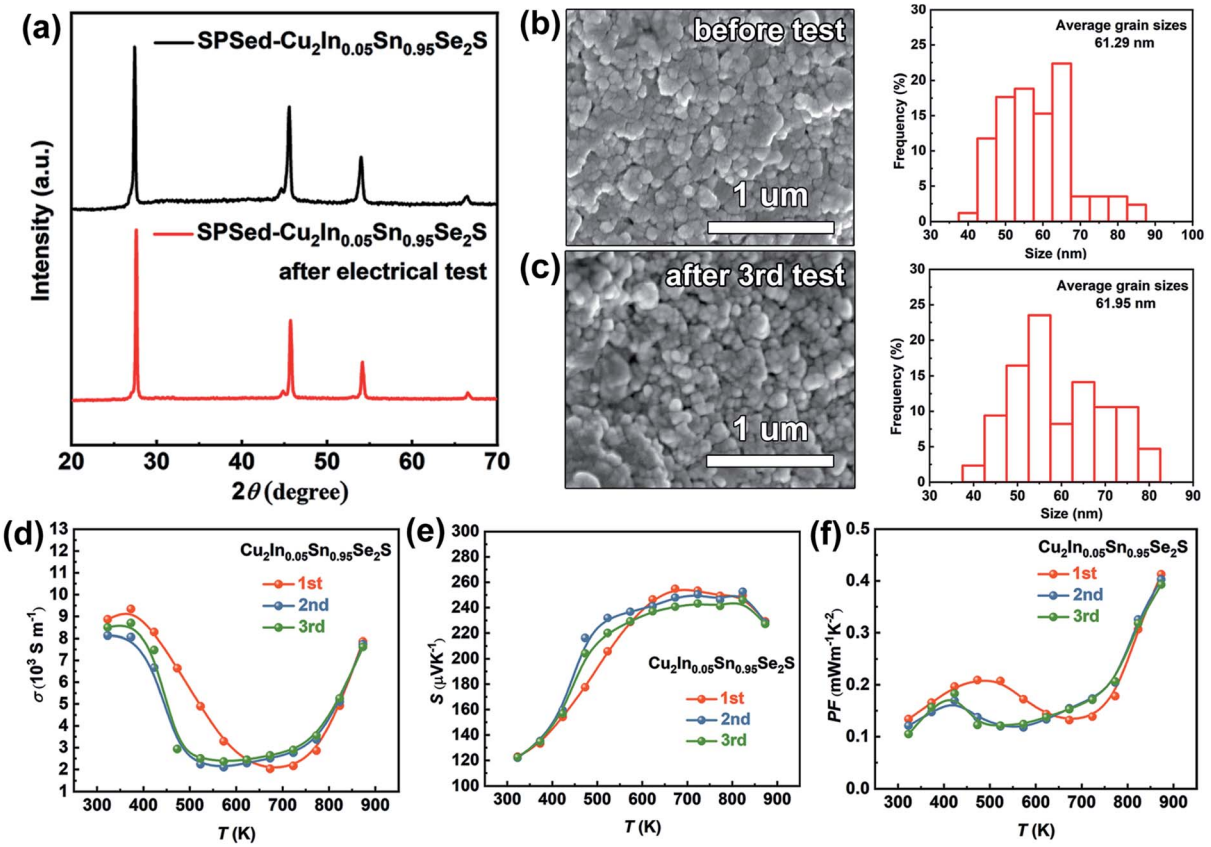

Fig. 6 The thermal stability tests for $Cu_2In_{0.05}Sn_{0.95}Se_2S$. (a) XRD patterns before testing and after the 3rd electrical test. (b and c) SEM micrographs of sintered pellets before testing and after three rounds of electrical tests. (d–f) Cyclic tests of electrical conductivity σ, Seebeck coefficient S and power factor PF.

k_{lat} and carrier mobility (μ_H) at ~300 K in the monoclinic-phase $Cu_2Sn_{0.82}In_{0.18}Se_{2.7}S_{0.3}$ and $Cu_{1.85}Ag_{0.15}Sn_{0.9}In_{0.1}Se_3$ reported by Ming *et al.*[35] and Li *et al.*,[34] a relatively low k_{lat} and μ_H (Table S5†) are obtained in our cubic $Cu_2In_{0.06}Sn_{0.94}Se_2S$ sample due to the nano-grain size, which enhances the grain boundary scattering for the charge carrier. The ultralow k_{lat} can compensate for the deterioration in electrical conductivity, which can be understood from the quality factor,[65] $\beta = (\mu_H/k_{lat})(m_d^*/m_e)^{3/2}$ (Table S5†), taking into account the k_{lat} and μ_H in the numerator and denominator, respectively.

The reproducibility of thermoelectric performance for $Cu_{1.87}Ag_{0.13}(In_{0.06}Sn_{0.94})Se_2S$ is provided in Fig. S24.† Besides, the thermal stability is a critical concern for metastable phases in the thermoelectric community. Thus, the XRD patterns of SPSed-$Cu_2In_{0.05}Sn_{0.95}Se_2S$ before testing and after the 3rd electrical test were measured, and no change in phase structure is found (Fig. 6a). Additionally, after measuring the electrical properties three times, the SPSed-$Cu_2In_{0.05}Sn_{0.95}Se_2S$ sample could still maintain the same grain size (Fig. 6b and c). The electrical performance was re-measured three times for $Cu_2In_{0.05}Sn_{0.95}Se_2S$ and shows no deterioration (Fig. 6d–f).

3. Conclusions

In summary, we have successfully synthesized a high-entropy system, $Cu_{2-y}Ag_y(In_xSn_{1-x})Se_2S$ (x = 0–0.25, y = 0, 0.07, 0.13), by adopting a hot-injection strategy and characterized the thermoelectric properties of dense materials compacted from those nanoparticles. We propose a new synthetic route for compacting nanocrystals without eliminating long organic ligands and subsequently obtain a series of high-entropy multinary chalcogenide nanocrystals with a metastable cubic phase induced by size-driven structural stabilization. Through phase and entropy design, a high power factor (0.44 mW m^{-1} K^{-2}) and an ultralow thermal conductivity (0.25 W m^{-1} K^{-1}) are achieved at 873 K for the $Cu_{1.87}Ag_{0.13}(In_{0.06}Sn_{0.94})Se_2S$ sample. A high ZT of 1.52 is achieved which is about 204% higher than that of pristine Cu_2SnSe_3. This work provides a new strategy for stabilizing the metastable phase through ligand retention induced small size and may have broader application in various fields such as photocatalysis, electronic devices, and photovoltaics.

Data availability

Chemicals, preparation of Cu_2SnSe_3, Cu_2SnSe_2S, $Cu_2In_xSn_{1-x}Se_2S$, $Cu_3InSnSe_3S_2$ and $Cu_{2-y}Ag_y(In_{0.06}Sn_{0.94})Se_2S$ nanocrystals, spark plasma sintering, characterization, measurement of thermoelectric properties, DFT calculation, formation energy calculation, the calculation details of Lorentz factor (L) and density of states effective mass (m_d^*) *via* single parabolic band (SPB) model, the calculation details of heat capacity C_p *via* the Debye-3 Einstein model, crystal structure characterization,

microstructure and composition, electronic and phononic band structures and thermoelectric properties are available in the ESI.†

Author contributions

Wanjia Zhang: investigation, methodology, data curation, formal analysis, visualization, writing – original draft. Yue Lou: resources, supervision, writing – review & editing. Hongliang Dong: synchrotron X-ray diffraction testing. Fanshi Wu: formal analysis, DFT calculation, writing – original draft. Janak Tiwari: formal analysis, DFT calculation, writing – original draft. Zhan Shi: resources, writing – reviewing. Sokrates T. Pantelides: supervision, writing – reviewing. Tianli Feng: conceptualization, DFT calculation, writing – review & editing, supervision. Biao Xu: conceptualization, writing – review & editing, supervision, project administration, funding acquisition.

Conflicts of interest

The authors declare no competing financial interest.

Acknowledgements

B. X. is thankful for financial support from Jiangsu Specially Appointed Professorship, the Jiangsu Provincial Innovation and Entrepreneurship Doctor Program, and the 1000 Young Talents Program. Y. L. is thankful for financial support from the Jiangsu Provincial Innovation and Entrepreneurship Doctor Program (JSSCBS20210215). The support and resources from the Center for High-Performance Computing at the University of Utah and the National Energy Research Scientific Computing Center (NERSC) are gratefully acknowledged. We thank the staff of the BL17B1 beamline of the National Facility for Protein Science in Shanghai (NFPS) at the Shanghai Synchrotron Radiation Facility.

References

1 B. Hu, X.-L. Shi, J. Zou and Z.-G. Chen, *Chem. Eng. J.*, 2022, **437**, 135268.
2 L. Li, W. D. Liu, Q. Liu and Z. G. Chen, *Adv. Funct. Mater.*, 2022, **32**, 2200548.
3 Z.-G. Chen and W.-D. Liu, *J. Mater. Sci. Technol.*, 2022, **121**, 256–262.
4 W.-Y. Chen, X.-L. Shi, J. Zou and Z.-G. Chen, *Small Methods*, 2022, **6**, 2101235.
5 M. Li, M. Hong, M. Dargusch, J. Zou and Z.-G. Chen, *Trends Chem.*, 2021, **3**, 561–574.
6 Z.-Z. Luo, S. Cai, S. Hao, T. P. Bailey, I. Spanopoulos, Y. Luo, J. Xu, C. Uher, C. Wolverton, V. P. Dravid, Q. Yan and M. G. Kanatzidis, *Angew. Chem., Int. Ed.*, 2021, **60**, 268–273.
7 Q. Liu, Z. Zhao, Y. Lin, P. Guo, S. Li, D. Pan and X. Ji, *Chem. Commun.*, 2011, **47**, 964–966.
8 D. Sarkar, T. Ghosh, A. Banik, S. Roychowdhury, D. Sanyal and K. Biswas, *Angew. Chem., Int. Ed.*, 2020, **59**, 11115–11122.
9 Y. Pei, X. Shi, A. LaLonde, H. Wang, L. Chen and G. J. Snyder, *Nature*, 2011, **473**, 66–69.
10 J. P. Heremans, B. Wiendlocha and A. M. Chamoire, *Energy Environ. Sci.*, 2012, **5**, 5510–5530.
11 J. P. Heremans, V. Jovovic, E. S. Toberer, A. Saramat, K. Kurosaki, A. Charoenphakdee, S. Yamanaka and G. J. Snyder, *Science*, 2008, **321**, 554–557.
12 L. Hu, T. Zhu, X. Liu and X. Zhao, *Adv. Funct. Mater.*, 2014, **24**, 5211–5218.
13 L. Hu, Y. Luo, Y.-W. Fang, F. Qin, X. Cao, H. Xie, J. Liu, J. Dong, A. Sanson, M. Giarola, X. Tan, Y. Zheng, A. Suwardi, Y. Huang, K. Hippalgaonkar, J. He, W. Zhang, J. Xu, Q. Yan and M. G. Kanatzidis, *Adv. Energy Mater.*, 2021, **11**, 2100661.
14 Y. Kinemuchi, M. Mikami, K. Kobayashi, K. Watari and Y. Hotta, *J. Electron. Mater.*, 2010, **39**, 2059–2063.
15 K. Peng, H. Wu, Y. Yan, L. Guo, G. Wang, X. Lu and X. Zhou, *J. Mater. Chem. A*, 2017, **5**, 14053–14060.
16 X.-L. Shi, W.-D. Liu, M. Li, Q. Sun, S.-D. Xu, D. Du, J. Zou and Z.-G. Chen, *Adv. Energy Mater.*, 2022, **12**, 2200670.
17 M. Li, Q. Sun, S.-D. Xu, M. Hong, W.-Y. Lyu, J.-X. Liu, Y. Wang, M. Dargusch, J. Zou and Z.-G. Chen, *Adv. Mater.*, 2021, **33**, 2102575.
18 W.-D. Liu, Y. Yu, M. Dargusch, Q. Liu and Z.-G. Chen, *Renewable Sustainable Energy Rev.*, 2021, **141**, 110800.
19 W.-D. Liu, L. Yang and Z.-G. Chen, *Nano Today*, 2020, **35**, 100938.
20 Y. Sun, C.-A. Di, W. Xu and D. Zhu, *Adv. Electron. Mater.*, 2019, **5**, 1800825.
21 B. Bai, M. Xu, N. Li, W. Chen, J. Liu, J. Liu, H. Rong, D. Fenske and J. Zhang, *Angew. Chem., Int. Ed.*, 2019, **58**, 4852–4857.
22 H. F. Cheng, N. L. Yang, Q. P. Lu, Z. C. Zhang and H. Zhang, *Adv. Mater.*, 2018, **30**, 1707189.
23 J. Liu, J. Huang, W. Niu, C. Tan and H. Zhang, *Chem. Rev.*, 2021, **121**, 5830–5888.
24 Y. Chen, Z. Lai, X. Zhang, Z. Fan, Q. He, C. Tan and H. Zhang, *Nat. Rev. Chem.*, 2020, **4**, 243–256.
25 Y. Luo, T. Xu, Z. Ma, D. Zhang, Z. Guo, Q. Jiang, J. Yang, Q. Yan and M. G. Kanatzidis, *J. Am. Chem. Soc.*, 2021, **143**, 13990–13998.
26 S. Roychowdhury, T. Ghosh, R. Arora, U. V. Waghmare and K. Biswas, *Angew. Chem., Int. Ed.*, 2018, **57**, 15167–15171.
27 H. Zhu, T. Zhao, B. Zhang, Z. An, S. Mao, G. Wang, X. Han, X. Lu, J. Zhang and X. Zhou, *Adv. Energy Mater.*, 2021, **11**, 2003304.
28 L. Hu, Y. Zhang, H. Wu, J. Li, Y. Li, M. Mckenna, J. He, F. Liu, S. J. Pennycook and X. Zeng, *Adv. Energy Mater.*, 2018, **8**, 1802116.
29 B. Jiang, Y. Yu, J. Cui, X. Liu, L. Xie, J. Liao, Q. Zhang, Y. Huang, S. Ning, B. Jia, B. Zhu, S. Bai, L. Chen, S. J. Pennycook and J. He, *Science*, 2021, **371**, 830–834.
30 Y. Luo, S. Hao, S. Cai, T. J. Slade, Z. Z. Luo, V. P. Dravid, C. Wolverton, Q. Yan and M. G. Kanatzidis, *J. Am. Chem. Soc.*, 2020, **142**, 15187–15198.
31 H. Duan, Z. Cheng, Y. Xue, Z. Cui, M. Yang and S. Wang, *J. Electroanal. Chem.*, 2021, **882**, 115037.

32 M. Wang, Z. Cui, Y. Xue, A. Yan, X. Yu, X. Song and H. Li, *Electroanalysis*, 2019, **31**, 1316–1323.
33 C. Wang, Z. Cui, Y. Xue, Y. Wang, M. Wang, B. Ji, J. Chen, Y. Xue and L. Zhang, *Thermochim. Acta*, 2022, **708**, 179140.
34 Y. Li, G. Liu, T. Cao, L. Liu, J. Li, K. Chen, L. Li, Y. Han and M. Zhou, *Adv. Funct. Mater.*, 2016, **26**, 6025–6032.
35 H. Ming, G. Zhu, C. Zhu, X. Qin, T. Chen, J. Zhang, D. Li, H. Xin and B. Jabar, *ACS Nano*, 2021, **15**, 10532–10541.
36 H. Ming, C. Zhu, X. Qin, J. Zhang, D. Li, B. Zhang, T. Chen, J. Li, X. Lou and H. Xin, *ACS Appl. Mater. Interfaces*, 2020, **12**, 19693–19700.
37 E. J. Skoug, J. D. Cain and D. T. Morelli, *J. Alloys Compd.*, 2010, **506**, 18–21.
38 R. Ma, G. Liu, Y. Li, J. Li, K. Chen, Y. Han, M. Zhou and L. Li, *J. Asian Ceram. Soc.*, 2018, **6**, 13–19.
39 X. Cheng, Z. Li, Y. You, T. Zhu, Y. Yan, X. Su and X. Tang, *ACS Appl. Mater. Interfaces*, 2019, **11**, 24212–24220.
40 Y. Zhou, H. Wu, D. Wang, L. Fu, Y. Zhang, J. He, S. J. Pennycook and L. D. Zhao, *Mater. Today Phys.*, 2018, **7**, 77–88.
41 G. Marcano, C. Rincón, S. A. López, G. Sánchez Pérez, J. L. Herrera-Pérez, J. G. Mendoza-Alvarez and P. Rodríguez, *Solid State Commun.*, 2011, **151**, 84–86.
42 H. Ming, C. Zhu, X. Qin, B. Jabar, T. Chen, J. Zhang, H. Xin, D. Li and J. Zhang, *Nanoscale*, 2021, **13**, 4233–4240.
43 Y. Lou, W. Zhao, C. Li, H. Huang, T. Bai, C. Chen, C. Liang, Z. Shi, D. Zhang, X.-B. Chen and S. Feng, *ACS Appl. Mater. Interfaces*, 2017, **9**, 18046–18053.
44 Y. Liu, M. Calcabrini, Y. Yu, S. Lee, C. Chang, J. David, T. Ghosh, M. C. Spadaro, C. Xie, O. Cojocaru-Mirédin, J. Arbiol and M. Ibáñez, *ACS Nano*, 2022, **16**, 78–88.
45 F.-J. Fan, L. Wu and S.-H. Yu, *Energy Environ. Sci.*, 2014, **7**, 190–208.
46 X. Wang, X. Liu, D. Yin, Y. Ke and M. T. Swihart, *Chem. Mater.*, 2015, **27**, 3378–3388.
47 W. W. Yu, Y. A. Wang and X. Peng, *Chem. Mater.*, 2003, **15**, 4300–4308.
48 M. E. Norako, M. J. Greaney and R. L. Brutchey, *J. Am. Chem. Soc.*, 2012, **134**, 23–26.
49 J. Jeong, H. Chung, Y. C. Ju, J. Moon, J. Roh, S. Yoon, Y. R. Do and W. Kim, *Mater. Lett.*, 2010, **64**, 2043–2045.
50 M. Beekman, D. T. Morelli and G. S. Nolas, *Nat. Mater.*, 2015, **14**, 1182–1185.
51 *CRC Handbook of Thermoelectrics*, ed. G. A. Slack and D. M. Rowe, CRC Press, Boca Raton, FL, USA, 1995.
52 M. B. Sigman, A. Ghezelbash, T. Hanrath, A. E. Saunders, F. Lee and B. A. Korgel, *J. Am. Chem. Soc.*, 2003, **125**, 16050–16057.
53 W. P. Lim, C. T. Wong, S. L. Ang, H. Y. Low and W. S. Chin, *Chem. Mater.*, 2006, **18**, 6170–6177.
54 Y. Yu, C. Zhou, S. Zhang, M. Zhu, M. Wuttig, C. Scheu, D. Raabe, G. J. Snyder, B. Gault and O. Cojocaru-Mirédin, *Mater. Today*, 2020, **32**, 260–274.
55 S. Roychowdhury, T. Ghosh, R. Arora, M. Samanta, L. Xie, N. K. Singh, A. Soni, J. He, U. V. Waghmare and K. Biswas, *Science*, 2021, **371**, 722–727.
56 Q. D. Gibson, T. Zhao, L. M. Daniels, H. C. Walker, R. Daou, S. Hébert, M. Zanella, M. S. Dyer, J. B. Claridge, B. Slater, M. W. Gaultois, F. Corà, J. Alaria and M. J. Rosseinsky, *Science*, 2021, **373**, 1017–1022.
57 W. Lin, J. He, X. Su, X. Zhang, Y. Xia, T. P. Bailey, C. C. Stoumpos, G. Tan, A. J. E. Rettie, D. Y. Chung, V. P. Dravid, C. Uher, C. Wolverton and M. G. Kanatzidis, *Adv. Mater.*, 2021, **33**, 2104908.
58 X. Shi, L. Xi, J. Fan, W. Zhang and L. Chen, *Chem. Mater.*, 2010, **22**, 6029–6031.
59 M. K. Jana, K. Pal, A. Warankar, P. Mandal, U. V. Waghmare and K. Biswas, *J. Am. Chem. Soc.*, 2017, **139**, 4350–4353.
60 J. L. Baker, J. T. White, A. Chen, T. Ulrich, R. R. Roback and H. Xu, *J. Nucl. Mater.*, 2021, **557**, 153282.
61 B. Koley, A. Lakshan, P. R. Raghuvanshi, C. Singh, A. Bhattacharya and P. P. Jana, *Angew. Chem., Int. Ed.*, 2021, **60**, 9106–9113.
62 R. Liu, H. Chen, K. Zhao, Y. Qin, B. Jiang, T. Zhang, G. Sha, X. Shi, C. Uher, W. Zhang and L. Chen, *Adv. Mater.*, 2017, **29**, 1702712.
63 G. Yang, L. Sang, F. F. Yun, D. R. G. Mitchell, G. Casillas, N. Ye, K. See, J. Pei, X. Wang, J.-F. Li, G. J. Snyder and X. Wang, *Adv. Funct. Mater.*, 2021, **31**, 2008851.
64 M. Li, D. L. Cortie, J. Liu, D. Yu, S. M. K. N. Islam, L. Zhao, D. R. G. Mitchell, R. A. Mole, M. B. Cortie, S. Dou and X. Wang, *Nano Energy*, 2018, **53**, 993–1002.
65 L.-P. Hu, T.-J. Zhu, Y.-G. Wang, H.-H. Xie, Z.-J. Xu and X.-B. Zhao, *NPG Asia Mater.*, 2014, **6**, e88.

Electronic Supporting Information

Phase-Engineered High-Entropy Metastable FCC $Cu_{2-y}Ag_y(In_xSn_{1-x})Se_2S$ Nanomaterials with High Thermoelectric Performance

Wanjia Zhang,[1,†] Yue Lou,[1,†] Hongliang Dong,[2] Fanshi Wu,[1] Janak Tiwari,[3] Zhan Shi,[4] Tianli Feng,[3] Sokrates T. Pantelides[5] and Biao Xu*[1]*

W. J. Zhang, Y. Lou, F. S. Wu, B. Xu

Department of Chemistry and Chemical Engineering, Nanjing University of Science and Technology, Nanjing, Jiangsu 210094, P.R. China

H. L. Dong

Center for High Pressure Science and Technology Advanced Research, Shanghai 201203, China

J. Tiwari, T. Feng

Department of Mechanical Engineering, The University of Utah, Salt Lake City, UT 84112, USA

Z. Shi

State Key Laboratory of Inorganic Synthesis and Preparative Chemistry, College of Chemistry, Jilin University, Changchun 130012, P.R. China

S. T. Pantelides

Department of Physics and Astronomy and Department of Electrical and Computer Engineering, Vanderbilt University, Nashville, TN 37235, USA

† These two authors contributed equally

*Corresponding Authors:

louyue@njust.edu.cn (Yue Lou)

xubiao@njust.edu.cn (Biao Xu)

Table of Contents

Experimental Procedures

Chemicals. Oleylamine (OAm, 80~90%) and 1-dodecanethiol (DDT, 98%) were purchased from Shanghai Macklin Biochemical Technology Co., Ltd. Tin chloride dehydrate ($SnCl_2{\cdot}2H_2O$, 99.99%), indium chloride ($InCl_3$, 99.99%) and copper chloride (CuCl, 99.95%) were obtained from Aladdin Reagent Co. Ltd. Diphenyl diselenide (97%) was purchased from Energy Chemical. Silver nitrate ($AgNO_3$) and ethanol were obtained from Sinopharm Chemical Reagent Co., Ltd and Nanjing Chemical Reagent Co., Ltd. All chemicals were directly used without any purifying treatments.

Preparation of Cu_2SnSe_3 nanocrystals. Solution A: Diphenyl diselenide/OAm solution was prepared by dissolving diphenyl diselenide (2.3410 g, 7.5 mmol) in OAm (30 mL) at room temperature through sonicating for about 15 minutes. Solution B: CuCl (0.8910 g, 9 mmol), $SnCl_2{\cdot}2H_2O$ (0.6770 g, 3 mmol) and OAm (120 mL) were mixed in a 500 mL three-neck flask. The mixture was degassed at room temperature for several minutes followed by purging with N_2 under magnetic stirring. Subsequently, the mixture was heated to 230 °C, and solution A was rapidly injected into the mixture. Finally, the mixture was heated to 240 °C and held for 30min. After being cooled to room temperature naturally, the products were washed with ethanol and dried under a vacuum.

Preparation of Cu_2SnSe_2S nanocrystals. All the steps and parameters are the same as the preparation of Cu_2SnSe_3, except for the addition of DDT (15 mL) in Solution B.

Preparation of $Cu_2In_xSn_{1-x}Se_2S$ and $Cu_3InSnSe_3S_2$ nanocrystals. All the steps and parameters are the same as the preparation of Cu_2SnSe_2S, except for the addition of $InCl_3$ (3x mmol) in Solution B and the corresponding decrease in $SnCl_2{\cdot}2H_2O$ amount.

Preparation of $Cu_{2-y}Ag_y(In_{0.06}Sn_{0.94})Se_2S$ nanocrystals. All the steps and parameters are the same as the preparation of $Cu_2In_xSn_{1-x}Se_2S$, except for the addition of $AgNO_3$ and the corresponding decrease in CuCl amount.

Spark Plasma Sintering. The dense bulk matrixes compacted from nanocrystals were prepared by spark plasma sintering (SPS) system (LABOX-110, Sinter Land) at 673 K with an axial compressive stress of 50 MPa for 10 min under vacuum. The obtained pellets were then cut into a 3 × 3 × 10 mm^3 rectangular bar and into a ∅10 × 1.5 mm disk.

Characterization. Synchrotron X-ray diffraction data were measured at BL17b in an energy state of 20 keV (0.62 Å). The pair distribution function G(r), correction, background subtraction, and sample absorption were completed by employing PDFgetX.[1] Structure refinements were accomplished by using PDFgui.[2] The crystalline phase of the samples was measured by powder X-ray diffraction (XRD; D8 ADVANCE, Bruker, Germany) with Cu Kα radiation (λ = 1.5418

Å) at a voltage of 40 kV and current of 40 mA. The microstructure of nanomaterials was investigated by transmission electron microscopy (TEM) and high-resolution transmission electron microscopy (HRTEM), taken by a Talos F200s transmission electron microscope operated at 200 kV. Elemental mapping images were acquired at the same instrument. Energy dispersive spectroscopy (EDS; JEOL JSM-6700F) was used for chemical composition analysis under an acceleration voltage of 10 kV. Atomic-resolution scanning transmission electron microscopy (STEM) images and energy-dispersive spectrometry (EDS) maps were acquired on an FEI-Titan Cubed Themis G2 300. STEM high angle annular dark field (STEM-HAADF) images were taken using an annular-type detector. The microstructure of the SPSed-samples pellets was characterized by a scanning electron microscope (SEM; FEI Scios 2 HiVac). X-ray photoelectron spectroscopy (XPS) was recorded by a PHI5000 Versa Probe system (ULVAC-PHI, Japan) with the monochromatic Al Kα line as the X-ray source. Atomic-scale composition analysis was conducted using atom probe tomography (APT). APT measurements were performed on a local electrode atom probe (LEAPTM 4000X Si, CAMECA) by applying 10-ps, 10-pJ ultraviolet (wavelength = 355 nm) laser pulses with a detection rate of 1 ion per 100 pulses on average, a pulse repetition rate of 200 kHz at a base temperature of 40 K, and an ion flight path of 160 mm. The corresponding 3D reconstructions and data analysis were processed using the IVASTM 3.8.0. Oxygen nitrogen hydrogen analyzer (ONH836) and carbon-sulfur analyzer (USA, LECO, CS844) were used for measurement of hydrogen and carbon concentrations in sintered nanomaterials.

Measurement of thermoelectric properties. The electrical conductivity and Seebeck coefficient were measured simultaneously by the static direct current method and four-probe method (CTA-3S, CRYALL). The measuring uncertainty of σ and S was ~ 5%. The thermal conductivity was calculated by $\kappa = C_p \cdot \rho \cdot D$, in which the specific heat at constant pressure (C_p) was obtained by using a differential scanning calorimetry thermalanalyzer (DSC 404 F3, NETZSCH), the pellet density (ρ) was calculated by Archimedes method and the thermal diffusivity (D) was measured using the laser flash method (Discovery Xeon Flash, TA Instrument). The measurement uncertainty of thermal conductivity κ was estimated to be within 10%, and thus the combined uncertainty for all measurements involved in ZT determination is below 20%. Charge carrier concentration (n_H) and Hall mobility (μ_H) were determined from the Hall coefficient (R_H) measurement using the Van der Pauw method under a reversible magnetic field of 1.5 T (Lake Shore 8400 Series, Model 8404, USA), and from $n_H = 1/eR_H$ and $\mu_H = \sigma R_H$, respectively. Low-temperature constant-pressure heat capacities (C_p) were measured using a Quantum Design Physical Properties Measurement System (QD-PPMS) with logarithmic T

spacings over 2 – 250 K repeating three times at each temperature point. Thermogravimetric analysis (TGA) was carried out on a thermal gravimetric analyzer (TGA 5500).

DFT calculation.

Electronic band structures: All calculations were performed within the first-principles density functional theory (DFT) formalism as implemented in the Vienna Ab-initio Simulation Package (VASP).[3] The structural optimizations and self-consistent calculations were carried out using the Perdew-Burke-Ernzerhof (PBE) generalized gradient approximation exchange functional plus the effective Hubbard *U* of the Dudarev et al's approach.[4] In this work, the on-site effective *U* = 10 eV was introduced to describe the localization characteristic of copper's 3d block. The cutoff energy was set to 500 eV and the energy conversion criterion of 1×10^{-6} eV per atom was used for the calculation of the electronic band structure. In the structural optimization, we constrained the cell parameters onto the experimental data and optimized the atomic coordinates until the Hellman-Feynman forces fell below 10^{-3} eV/Å.

Phonon band structures: The phonon band structure, group velocity, specific heat, density of states are calculated by using Phonopy[5] and VASP. The plane-wave energy cutoff is 500 eV. The energy convergence threshold is 10^{-8} eV per atom. The cubic Cu_2SnSe_3, under virtual crystal approximation, has 2 atoms per primitive cell. The monoclinic Cu_2SnSe_3 has 12 atoms per primitive cell. In the primitive cell relaxations, we use 10^{-6} and 10^{-4} eV/Å for the force convergence threshold for the cubic and monoclinic Cu_2SnSe_3, respectively. The **k**-mesh during the primitive cell relaxations are 16×16×16 and 9×9×9 for the cubic and monoclinic Cu_2SnSe_3, respectively. 4×4×4 and 3×3×3 supercells are used for the calculation of phonon dispersion for cubic and monoclinic Cu_2SnSe_3, respectively. The **k**-mesh used in the supercell calculations is 3×3×3.

Formation Energy Calculation. In general, the formation energy for a compound is calculated by using the equation given below:[6]

$$\Delta H_f = E_{tot} - \sum_i \mu_i x_i \qquad (S1)$$

where E_{tot} is the DFT total energy of the compound, μ_i is the chemical potential of element *i*, and x_i is the quantity of element *i* in the compound.

The calculation details of Lorentz factor (L) and density of states effective mass (m_d^*) via single parabolic band (SPB) model. In the case of electron scattering by the acoustical vibrations of the lattice atoms, the Lorenz number can be expressed as:[7]

$$L = \left(\frac{k_B}{e}\right)^2 \frac{3F_0(\eta)F_2(\eta) - 4F_1^2(\eta)}{F_0^2(\eta)} \qquad (S2)$$

Assuming the acoustic scattering for all investigated samples is prominent (λ=0), the m_d^* can be acquired from the experimental data *S* and *p* by using the following equations:

$$S = \frac{k_B}{e}\left[\frac{(\lambda+2)F_{(\lambda+1)}(\eta)}{(\lambda+1)F_\lambda(\eta)} - \eta\right] \quad (S3)$$

$$m_d^* = \frac{h^2}{2k_BT}\left(\frac{p}{4\pi F_{1/2}(\eta)}\right)^{2/3} \quad (S4)$$

$$F_j(\eta) = \int_0^\infty \frac{x^j}{1-e^{x-\eta}}dx \quad (S5)$$

where $F_j(\eta)$ is the Fermi integral of order j, η is the reduced Fermi level E_f/κ_BT and h is the Planck constant.

The calculation details of heat capacity C_p via the Debye-3 Einstein model. The plot of C_p vs *T* could be well fitted to a sum of Debye and Einstein models ranging from 100-200 K as the following equation[8-10]:

$$C_{ph}(T) = 9R\frac{\sum_{i=1}^{3} a_i}{n-1}x_D^{-3}\int_0^{x_D}\frac{x^4e^x}{(e^x-1)^2}dx + 3R\sum_{i=1}^{3}[a_i\frac{x_{E_i}^2e^{xE_i}}{(e^{xE_i}-1)^2}] \quad (S6)$$

where $x_D = \theta_D/T$, $x_E = \theta_E/T$, and θ_D, θ_E are the Debye and Einstein temperatures, respectively. The constant *R* is the molar gas constant. The parameter *n* is the number of atoms per molecular formula. The letters are adjustable, and the subscript *i* represents the degeneracy of the multiple optical branches. The various fitting parameters are listed in Table S4.

Results and Discussion

1. Crystal structure characterization

As shown in Fig. S1, for Cu_2SnSe_3, Cu_2SnSe_2S, $Cu_2In_xSn_{1-x}Se_2S$ (x=0.06, 0.14, 0.25), the peak at 26.8° can be indexed to the (111) plane of the cubic structure of $Cu_{1.8}Se$ phase, which indicates the existence of a small quantity of the second phase. And we can observe that $Cu_{1.8}Se$ phase disappeared when the amount of In increased, and finally $Cu_2In_{0.4}Sn_{0.6}Se_2S$ and $Cu_3InSnSe_3S_2$ nanocrystals without the second phase were obtained. This phenomenon demonstrates that the main reason of the formation of $Cu_{1.8}Se$ second phase is feed ratio of metal salts. When the amount of In is small, excess Se will reacted with Cu to obtain $Cu_{1.8}Se$.

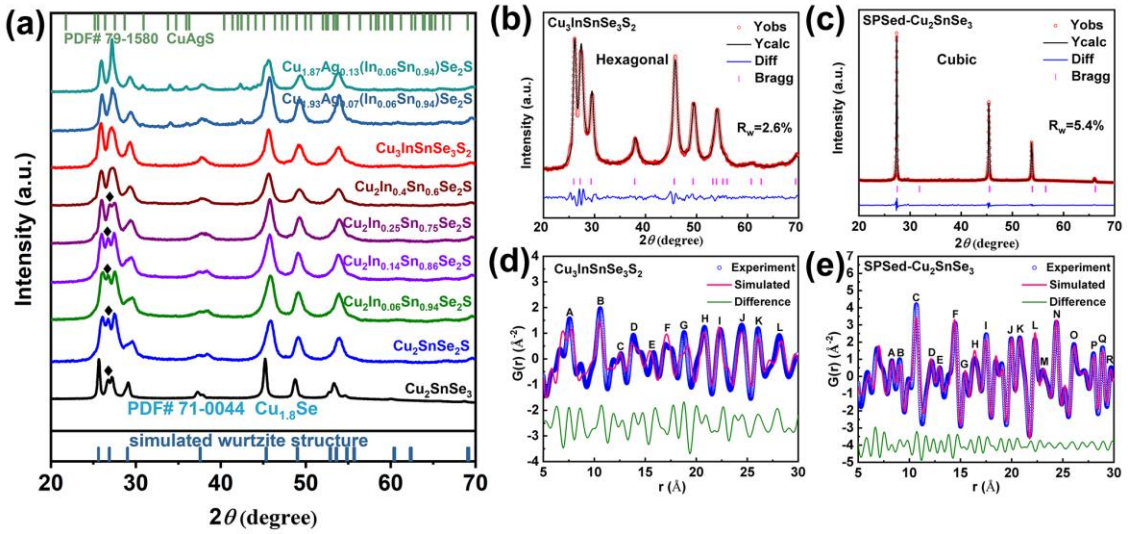

Fig. S1 (a) Powder X-ray diffraction (PXRD) patterns of solution-synthesized samples. Rietveld refinement results of (b) solution-synthesized $Cu_3InSnSe_3S_2$ and (c) SPSed-Cu_2SnSe_3. PDF fit to G(r) function at the range of 5-30 Å by using the hexagonal model for (d) solution-synthesized $Cu_3InSnSe_3S_2$ and cubic model for (e) SPSed-Cu_2SnSe_3.

Table S1. The cell parameters of solution-synthesized and SPSed-samples from Rietveld refinement data.

Parameter	Solution-synthesized $Cu_3InSnSe_3S_2$	SPSed-Cu_2SnSe_3	SPSed-$Cu_3InSnSe_3S_2$	SPSed-$Cu_{1.93}Ag_{0.07}(In_{0.06}Sn_{0.94})Se_2S$
space group	$P6_3mc$	Fm-3m	I-42m	Fm-3m
a	3.982 Å	5.6636 Å	5.6378 Å	5.6421 Å
b	3.982 Å	5.6636 Å	5.6378 Å	5.6421 Å
c	6.578 Å	5.6636 Å	11.2620 Å	5.6421 Å
α	90°	90°	90°	90°
β	90°	90°	90°	90°
γ	120°	90°	90°	90°

As demonstrated in Fig. S2, metastable wurtzite Cu_2SnSe_3 nanocrystals with uniform size and morphology is firstly synthesized via colloid synthesis. Then S is incorporated into the anionic site and Ag, In are alloyed at the cationic site through well controlling the balance of precursors reactivity in colloidal synthesis. Subsequently, based on size reduction and entropy optimization engineering of our solution-synthesized nanocrystals, a series of high-entropy multinary chalcogenides nanostructured solid with metastable cubic phase are obtained, which is different from the conventional monoclinic phase synthesized via solid-state synthesis, as exemplified by melting. Besides, when the amount of indium increases to a certain amount, SPSed-$Cu_2In_{0.4}Sn_{0.6}Se_2S$ and SPSed-$Cu_3InSnSe_3S_2$ nanostructured solid have a tetragonal structure (space group *I*-42*m*), and this tetragonal unit cell can be approximately depicted as a 1x1x2 supercell of cubic Cu_2SnSe_3.

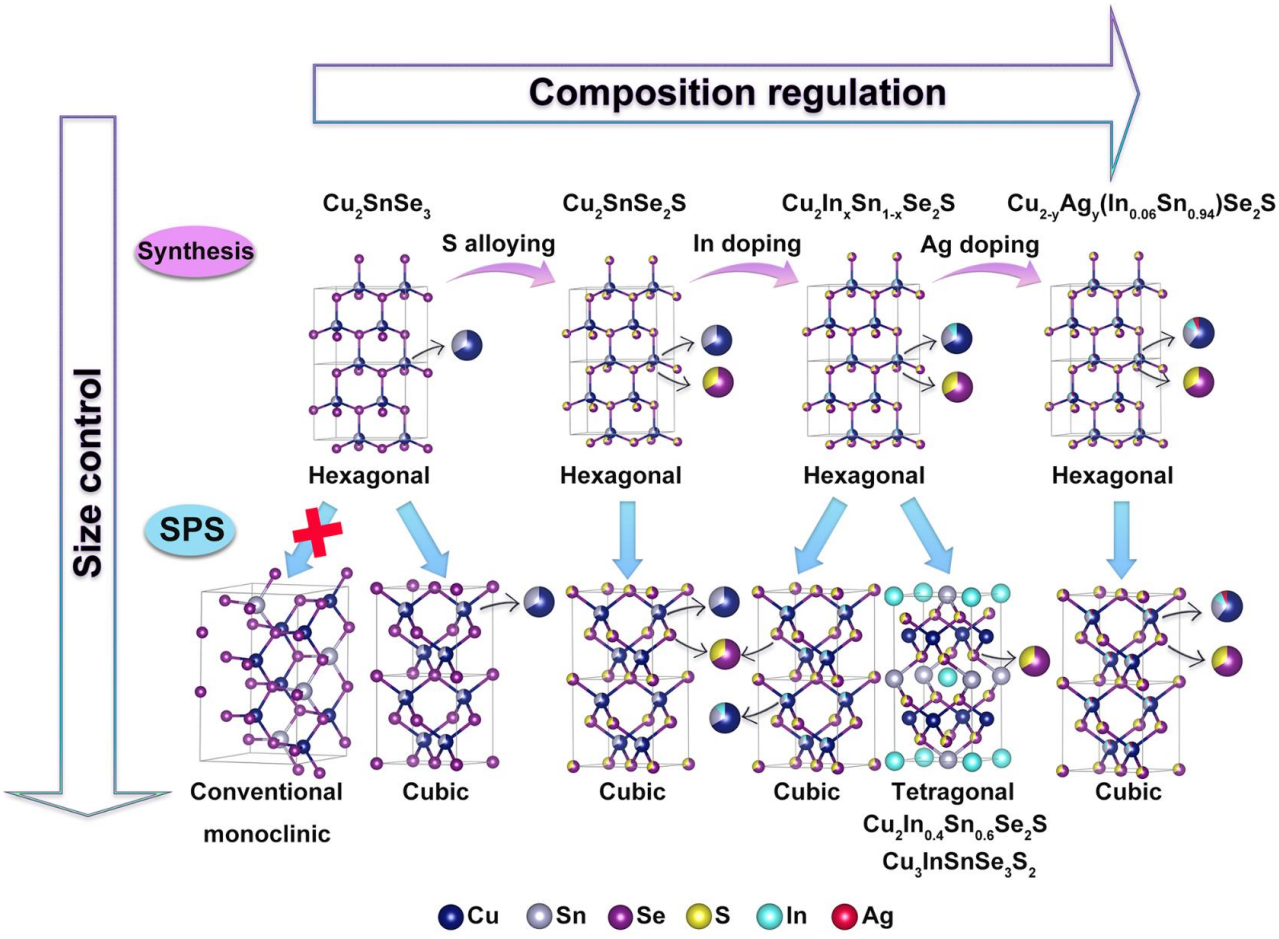

Fig. S2 Crystal structures for synthesized and SPSed-Cu_2SnSe_3, Cu_2SnSe_2S, $Cu_2In_xSn_{1-x}Se_2S$ (x=0.02-0.25), $Cu_2In_{0.4}Sn_{0.6}Se_2S$, $Cu_3InSnSe_3S_2$ and $Cu_{2-y}Ag_y(In_{0.06}Sn_{0.94})Se_2S$ (y=0.07, 0.13).

Table S2. Calculated formation energy (ΔH_f) for different phase structures via DFT using the Vienna ab initio simulation package (VASP).

Phase / Sample	Monoclinic ($eV \cdot atom^{-1}$)	Cubic ($eV \cdot atom^{-1}$)	Tetragonal ($eV \cdot atom^{-1}$)
SPSed-Cu_2SnSe_3	-2.4564	-2.4529	/
SPSed-Cu_2SnSe_2S	-2.5603	-2.5519	/
SPSed-$Cu_2In_{0.06}Sn_{0.94}Se_2S$	-2.5523	-2.5435	/
SPSed-$Cu_3InSnSe_3S_2$	-3.3915	-3.3863	-3.3994
SPSed-$Cu_{1.87}Ag_{0.13}(In_{0.06}Sn_{0.94})Se_2S$	-2.5816	-2.5730	/

Table S3. Table peaks assignment to the atomic pair in SPSed-Cu_2SnSe_3, solution-synthesized $Cu_3InSnSe_3S_2$, SPSed-$Cu_3InSnSe_3S_2$ and SPSed-$Cu_{1.93}Ag_{0.07}(In_{0.06}Sn_{0.94})Se_2S$, respectively. SPSed-$Cu_2SnSe_3$:

label	atomic pair	atomic pair distances(Å)
A	Se-Cu/(Sn)	8.26
B	Se-Se; Cu-Cu/(Sn); Sn-Sn	9.02
C	Se-Se	10.65
D	Se-Se; Cu-Cu/(Sn); Sn-Sn	12.16
E	Se-Cu/(Sn)	12.94
F	Se-Se; Cu-Cu/(Sn); Sn-Sn	14.43
G	Se-Se	15.42
H	Cu-Cu/(Sn); Sn-Sn	16.36
I	Se-Se; Cu-Cu/(Sn); Sn-Sn	17.50
J	Se-Se; Cu-Cu/(Sn); Sn-Sn	19.95
K	Cu-Cu/(Sn); Sn-Sn	20.80
L	Se-Se; Cu-Cu/(Sn); Sn-Sn	22.27
M	Se-Se; Se-Cu/(Sn)	23.05
N	Se-Se; Cu-Cu/(Sn); Sn-Sn	24.38
O	Se-Cu/(Sn)	26.10
P	Se-Se	28.00
Q	Se-Cu/(Sn)	28.87
R	Se-Cu/(Sn)	29.79

Solution-synthesized $Cu_3InSnSe_3S_2$:

label	atomic pair	atomic pair distances(Å)
A	Se-Se; S-S; Se-S	7.56
B	Se-Se; S-S; Se-S; Cu-Cu/(In)/(Sn); In-In/(Sn); Sn-Sn	10.57
C	Se-Cu/(In)/(Sn); S-Cu/(In)/(Sn);	12.62
D	Cu-Cu/(In)/(Sn); In-In/(Sn); Sn-Sn; Se-Cu/(In)/(Sn); S-Cu/(In)/(Sn)	13.83
E	Se-Cu/(In)/(Sn); S-Cu/(In)/(Sn)	15.80
F	Se-Se; S-S; Se-S; Se-Cu/(In)/(Sn); S-Cu/(In)/(Sn)	16.99
G	Cu-Cu/(In)/(Sn); In-In/(Sn); Sn-Sn	18.79
H	Se-Se; S-S; Se-S; Cu-Cu/(In)/(Sn); In-In/(Sn); Sn-Sn	20.79
I	Se-Se; S-S; Se-S; Cu-Cu/(In)/(Sn); In-In/(Sn); Sn-Sn	22.34
J	Cu-Cu/(In)/(Sn); In-In/(Sn); Sn-Sn; Se-Cu/(In)/(Sn); S-Cu/(In)/(Sn)	24.45
K	Se-Cu/(In)/(Sn); S-Cu/(In)/(Sn)	26.05
L	Se-Se; S-S; Se-S	28.15

SPSed-$Cu_3InSnSe_3S_2$:

label	atomic pair	atomic pair distances(Å)
A	S-In; Se-In	8.23
B	Se-Se; S-S; Se-S	9.01
C	S-In; Se-In; Cu-Cu; In-In	10.64
D	S-In; Se-In	12.17
E	S-In; Se-In	12.91
F	Se-Se; S-S; Se-S	14.40
G	S-Cu; Se-Cu	16.27
H	Se-Se; S-S; Se-S; In-In	17.44
I	Cu-In	19.88
J	In-In	20.74
K	Se-Se; S-S; Se-S; S-Cu; Se-Cu	22.20
L	Se-Se; S-S; Se-S	22.97
M	Se-Se; S-S; Se-S; S-In; Se-In	24.27
N	Cu-In	26.01
O	Cu-In	27.88
P	S-Cu; Se-Cu	28.79
Q	S-Cu; Se-Cu	29.61

SPSed-$Cu_{1.93}Ag_{0.07}(In_{0.06}Sn_{0.94})Se_2S$:

label	atomic pair	atomic pair distances(Å)
A	Se-Se; S-S; Se-S	6.89
B	Se-Cu/(In)/(Sn)/(Ag); S-Cu/(In)/(Sn)/(Ag)	8.33
C	Se-Se; S-S; Se-S; Cu-Cu/(In)/(Sn)/(Ag); In-In/(Sn)/(Ag); Sn-Sn/(Ag); Ag-Ag	9.07
D	Se-Se; S-S; Se-S	10.64
E	Se-Se; S-S; Se-S; Cu-Cu/(In)/(Sn)/(Ag); In-In/(Sn)/(Ag); Sn-Sn/(Ag); Ag-Ag	12.07
F	Se-Cu/(In)/(Sn)/(Ag); S-Cu/(In)/(Sn)/(Ag)	12.86
G	Se-Se; S-S; Se-S; Cu-Cu/(In)/(Sn)/(Ag); In-In/(Sn)/(Ag); Sn-Sn/(Ag); Ag-Ag	14.38
H	Cu-Cu/(In)/(Sn)/(Ag); In-In/(Sn)/(Ag); Sn-Sn/(Ag); Ag-Ag	16.45
I	Se-Se; S-S; Se-S; Cu-Cu/(In)/(Sn)/(Ag); In-In/(Sn)/(Ag); Sn-Sn/(Ag); Ag-Ag	17.43
J	Se-Se; S-S; Se-S; Cu-Cu/(In)/(Sn)/(Ag); In-In/(Sn)/(Ag); Sn-Sn/(Ag); Ag-Ag	19.93
K	Cu-Cu/(In)/(Sn)/(Ag); In-In/(Sn)/(Ag); Sn-Sn/(Ag); Ag-Ag	20.79
L	Se-Se; S-S; Se-S; Cu-Cu/(In)/(Sn)/(Ag); In-In/(Sn)/(Ag); Sn-Sn/(Ag); Ag-Ag	22.22
M	Se-Se; S-S; Se-S; Se-Cu/(In)/(Sn)/(Ag); S-Cu/(In)/(Sn)/(Ag)	23.02
N	Se-Se; S-S; Se-S; Cu-Cu/(In)/(Sn)/(Ag); In-In/(Sn)/(Ag); Sn-Sn/(Ag); Ag-Ag	24.32
O	Se-Cu/(In)/(Sn)/(Ag); S-Cu/(In)/(Sn)/(Ag)	26.02
P	Se-Se; S-S; Se-S	27.95
Q	Se-Cu/(In)/(Sn)/(Ag); S-Cu/(In)/(Sn)/(Ag)	28.84

2. Microstructure and composition

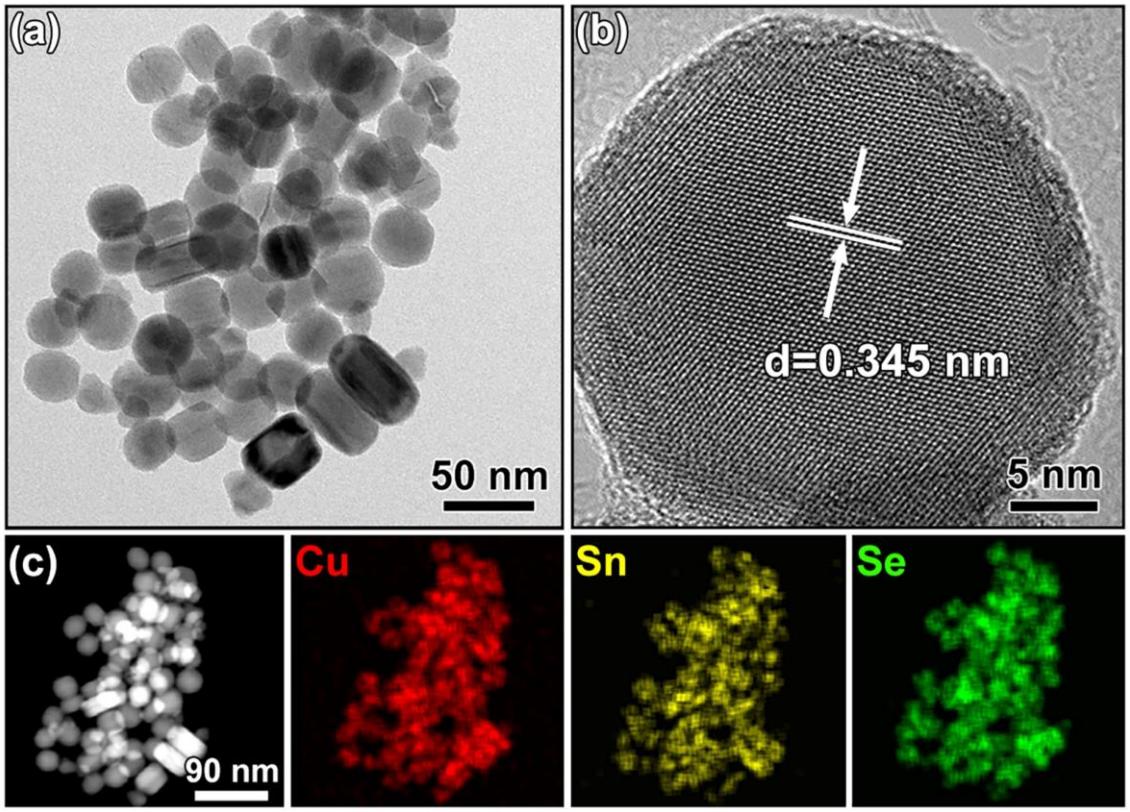

Fig. S3 (a) Low-magnification TEM image, (b) HRTEM image, (c) EDS elemental mapping images of solution-synthesized Cu_2SnSe_3.

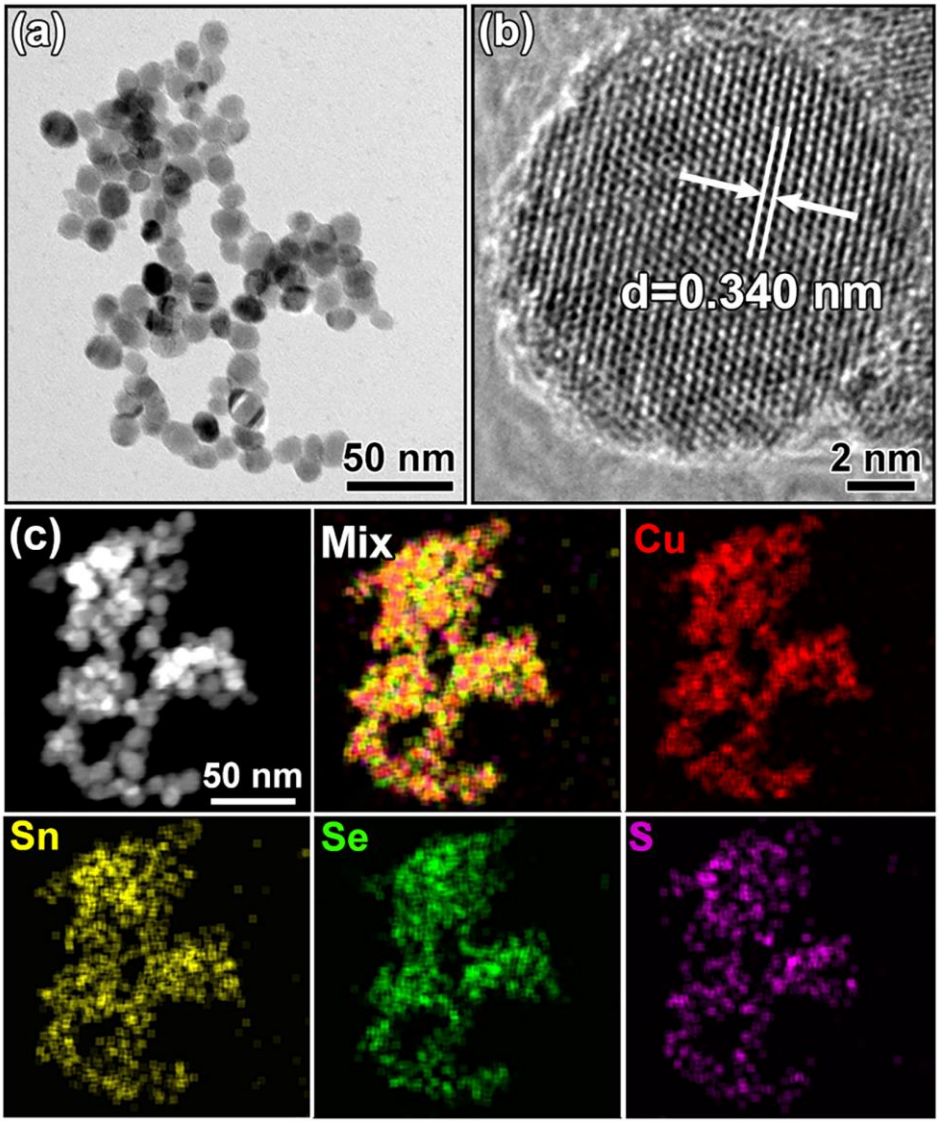

Fig. S4 (a) Low-magnification TEM image, (b) HRTEM image, (c) EDS elemental mapping images of solution-synthesized Cu_2SnSe_2S.

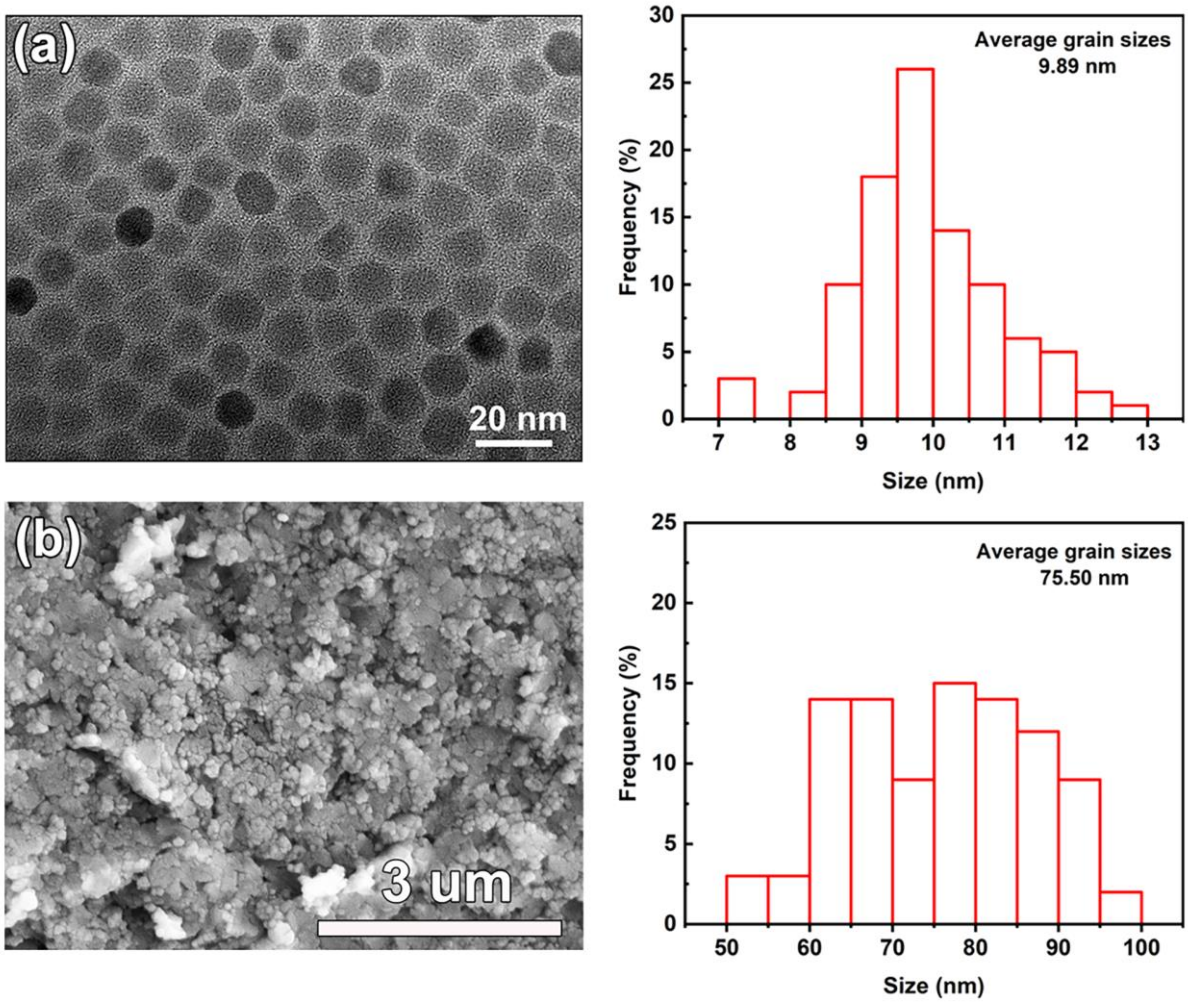

Fig. S5 (a) Low-magnification TEM image of solution-synthesized $Cu_3InSnSe_3S_2$ and (b) SEM micrograph of SPSed-$Cu_3InSnSe_3S_2$ sample.

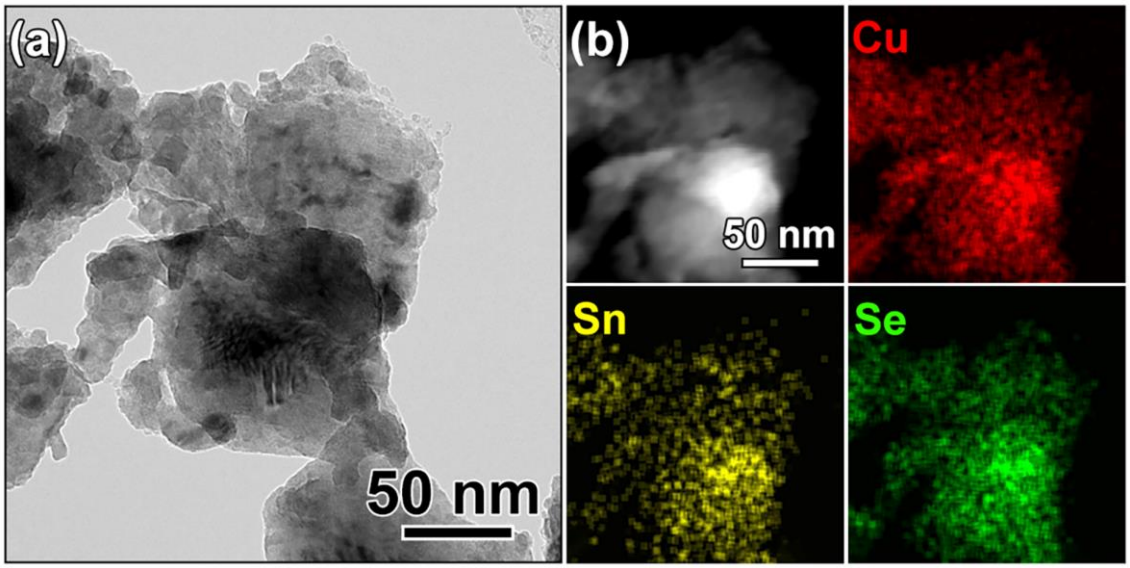

Fig. S6 (a) Low-magnification TEM image and (b) EDS elemental mapping images of SPSed-Cu_2SnSe_3.

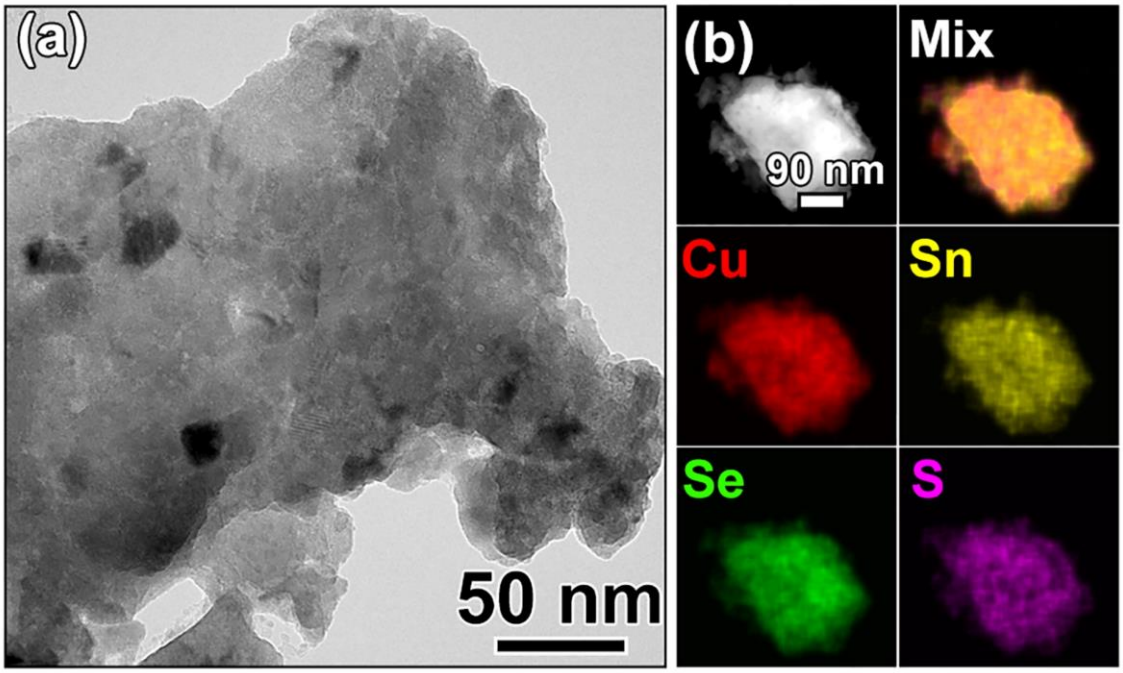

Fig. S7 (a) Low-magnification TEM image and (b) EDS elemental mapping images of SPSed-Cu_2SnSe_2S.

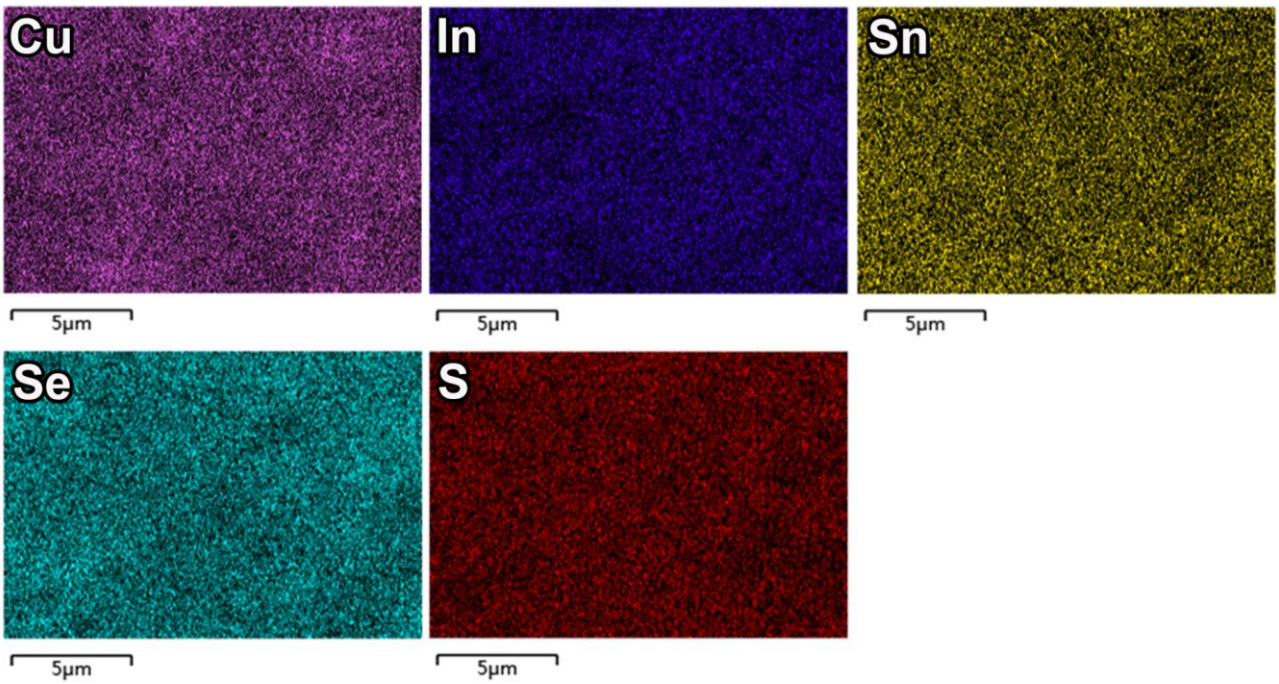

Fig. S8 The SEM/EDS mapping of SPSed-$Cu_3InSnSe_3S_2$.

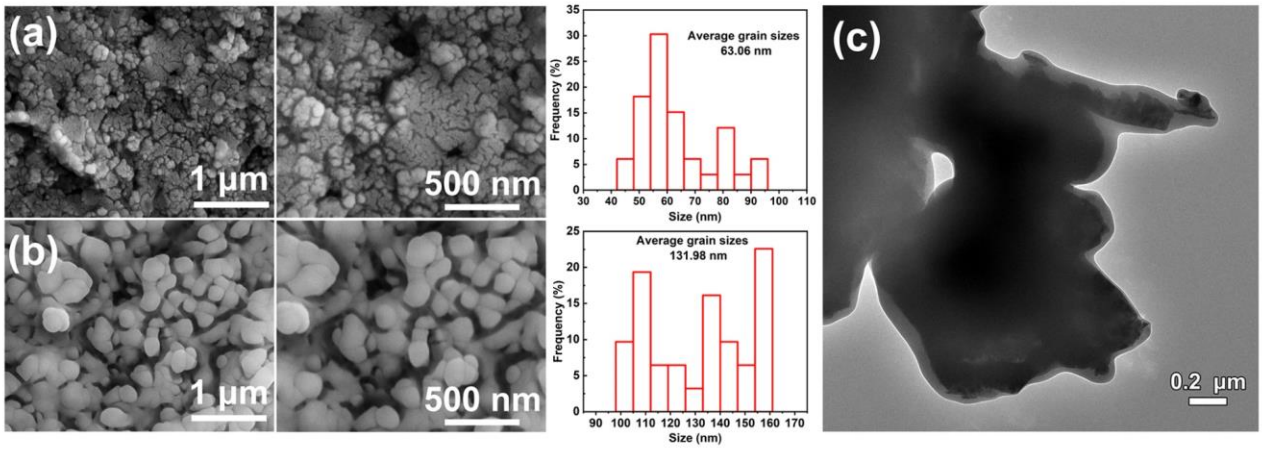

Fig. S9 SEM micrographs of (a) SPSed-$Cu_2In_{0.06}Sn_{0.94}Se_2S$ and (b) SPSed-$Cu_{1.87}Ag_{0.13}(In_{0.06}Sn_{0.94})Se_2S$ pellets. (c) The TEM image of SPSed-$Cu_{1.87}Ag_{0.13}(In_{0.06}Sn_{0.94})Se_2S$, exhibiting the organic hydrocarbons between nanocrystals of nanosructured solids during sintering process.

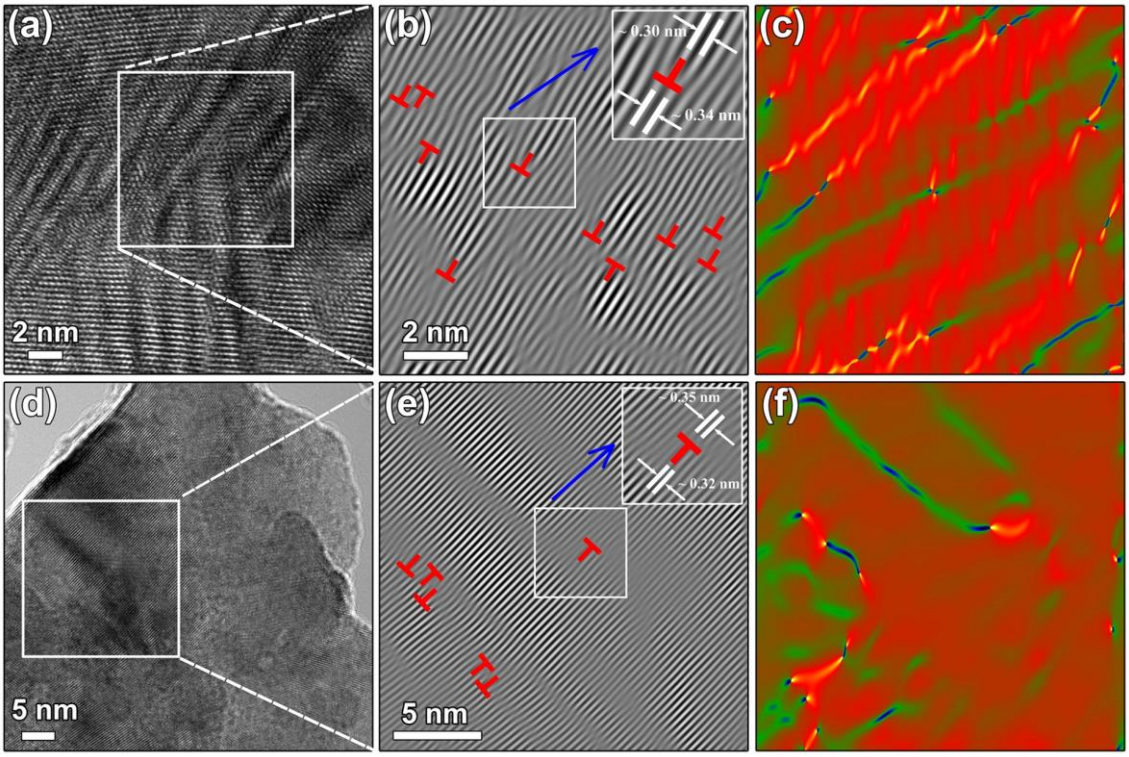

Fig. S10 HRTEM images of the dislocations in (a) SPSed-Cu_2SnSe_3 and (d) SPSed-Cu_2SnSe_2S samples. (b and e) The corresponding inverse FFT (IFFT) images of boxed region in (a) and (d), inset is the enlarged view of boxed region. (c and f) The corresponding strain mappings of (b) and (e), showing the dislocations cores with the high intensity.

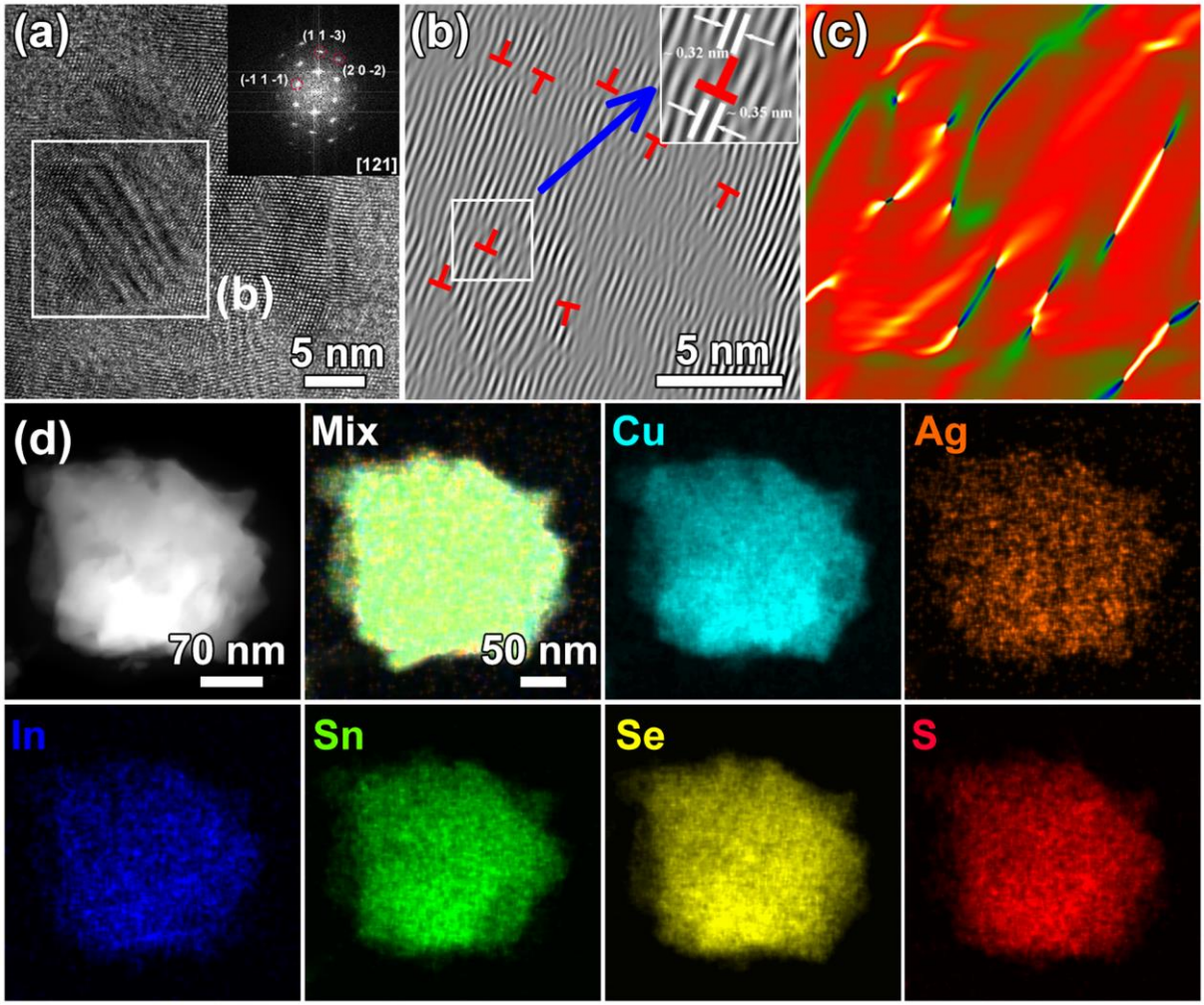

Fig. S11 HRTEM image of the dislocations in (a) SPSed-$Cu_{1.87}Ag_{0.13}(In_{0.06}Sn_{0.94})Se_2S$ sample, inset is the corresponding FFT along the [121] zone axis. (b) The corresponding inverse FFT (IFFT) image of boxed region in (a), inset is the enlarged view of boxed region. (c) The corresponding strain mapping of (b), showing the dislocations cores with high intensity. (d) EDS elemental mapping images of SPSed-$Cu_{1.87}Ag_{0.13}(In_{0.06}Sn_{0.94})Se_2S$ sample.

EDS analysis was used to quantify the elemental composition of solution-synthesized and SPSed-samples, as shown in Fig. S10. The EDS result of Cu_2SnSe_3 is shown in Fig. S10a, indicating that the atomic ratio of Cu: Sn: Se is 2.24: 1: 3.24. Then DDT was added as a sulfur source to prepare Cu_2SnSe_2S. The EDS spectra of $Cu_2In_{0.06}Sn_{0.94}Se_2S$ and SPSed-$Cu_2In_{0.06}Sn_{0.94}Se_2S$ are shown in Figs. S10c and f, proving the successful incorporation of In. And the composition of as-synthesized nanocrystals remains unchanged after the sintering process. Additionally, the In content in the nanocrystals increases almost linearly with increasing In content in the precursors. When a 1:1 ratio of $SnCl_2{\cdot}2H_2O$ to $InCl_3$ was used for the synthesis, the atom ratio of Cu: In: Sn: Se: S is around 3:1:1:3:2, which further verifies that the resulting products are $Cu_3InSnSe_3S_2$.

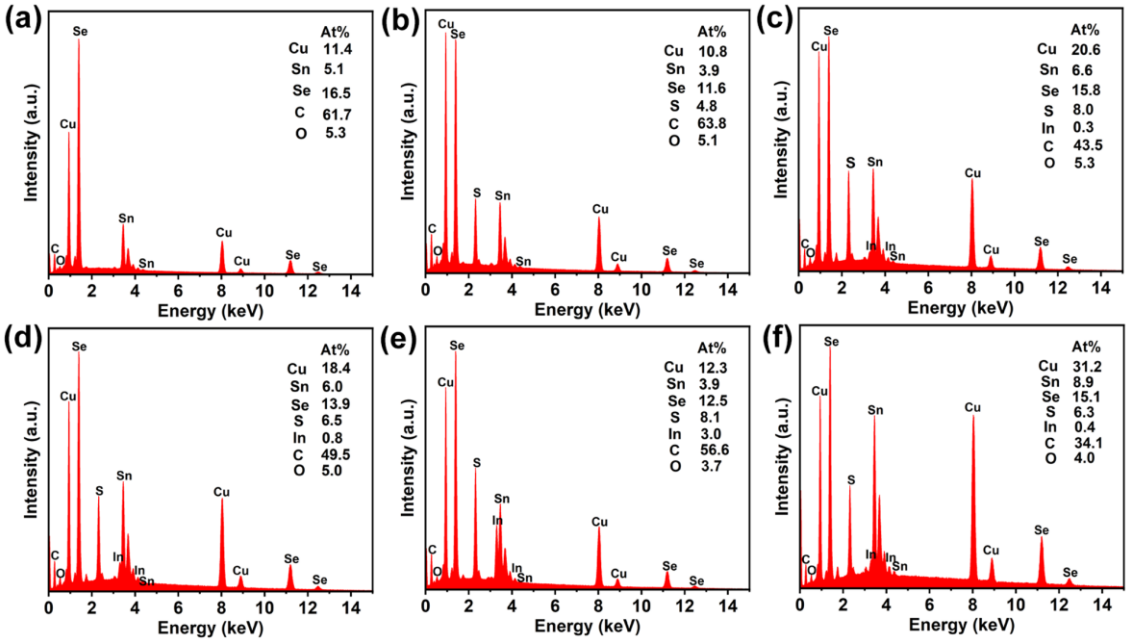

Fig. S12 EDS results of (a) solution-synthesized Cu_2SnSe_3, (b) solution-synthesized Cu_2SnSe_2S, (c) solution-synthesized $Cu_2In_{0.06}Sn_{0.94}Se_2S$, (d) solution-synthesized $Cu_2In_{0.14}Sn_{0.86}Se_2S$, (e) solution-synthesized $Cu_3InSnSe_3S_2$ and (f) SPSed-$Cu_2In_{0.06}Sn_{0.94}Se_2S$.

X-ray photoelectron spectroscopy (XPS) was performed to disclose the valence states of each element on the surface in the solution-synthesized $Cu_2In_{0.06}Sn_{0.94}Se_2S$ and SPSed-$Cu_2In_{0.06}Sn_{0.94}Se_2S$, as shown in Fig. S11. No peaks of other elements than Cu, In, Sn, Se, S, C, and O are observed in XPS survey spectrum, which agrees well with the EDS results. The dual peaks of Cu 2p for $Cu_2In_{0.06}Sn_{0.94}Se_2S$ at 932.0 eV and 951.8 eV with a separation of 19.8 eV reveal the presence of Cu with a valence of +1, and no satellite peak caused by Cu with +2 valence is found.[11-13] It is worth mentioning that the valence state of Cu changed before and after sintering. The binding energy of SPSed-$Cu_2In_{0.06}Sn_{0.94}Se_2S$ at the Cu 2p region could be divided into four peaks. The peaks located at 932.3 eV and 952.3 eV are associated with Cu^+ $2p_{3/2}$ and $2p_{1/2}$, respectively, and the peaks located at 934.5 eV and 954.7 eV are assigned to Cu^{2+} $2p_{3/2}$ and $2p_{1/2}$, respectively.[14] The In 3d peaks of $Cu_2In_{0.06}Sn_{0.94}Se_2S$ and SPSed-$Cu_2In_{0.06}Sn_{0.94}Se_2S$ at 444.6 eV and 452 eV can be assigned to In with a valence of +3.[11-13] The peaks of Sn 3d for $Cu_2In_{0.06}Sn_{0.94}Se_2S$ and SPSed-$Cu_2In_{0.06}Sn_{0.94}Se_2S$ at 486.3 eV and 494.7 eV are characteristic for Sn with a valence of +4.[11-13] The Se 3d peak at 54 eV for $Cu_2In_{0.06}Sn_{0.94}Se_2S$ and SPSed-$Cu_2In_{0.06}Sn_{0.94}Se_2S$ correspond to Se with a valence of -2.[15,16] In addition, we can find that another peak located at 58.8 eV for $Cu_2In_{0.06}Sn_{0.94}Se_2S$ was attributed to Se substance,[14] demonstrating excessive Se in raw materials. However, the Se substance peak disappears after sintering, indicating that part of Se volatilizes or reacts with Cu to form $Cu_{1.8}Se$ during the sintering process, which explains the existence of Cu^{2+} in the SPSed-sample. The corresponding peaks for the S $2p_{3/2}$ and $2p_{1/2}$ orbitals of bivalent sulfide ions (S^{2-}) are observed at 160.5 and 165.4 eV of $Cu_2In_{0.06}Sn_{0.94}Se_2S$ and SPSed-$Cu_2In_{0.06}Sn_{0.94}Se_2S$, respectively.[12]

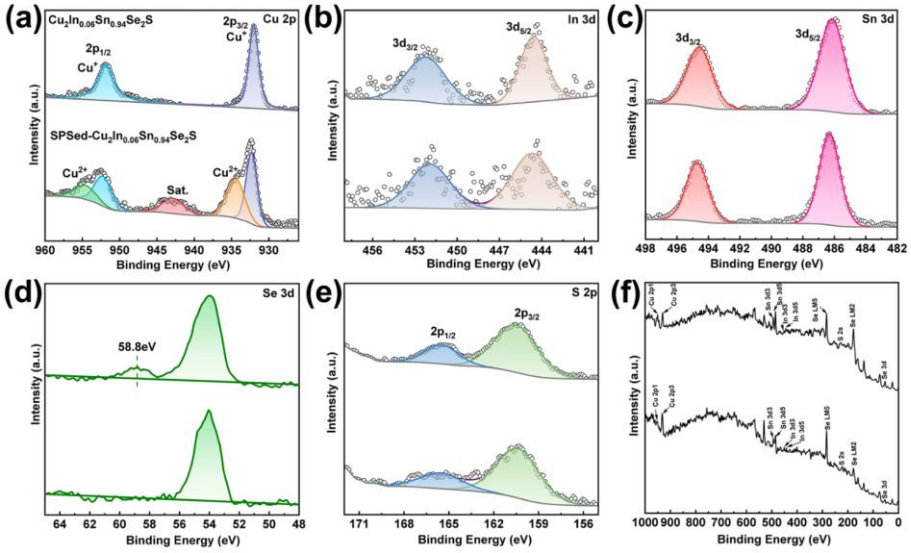

Fig. S13 XPS spectra of the solution-synthesized $Cu_2In_{0.06}Sn_{0.94}Se_2S$ and SPSed-$Cu_2In_{0.06}Sn_{0.94}Se_2S$ (a) Cu 2p, (b) In 3d, (c) Sn 3d, (d) Se 3d, (e) S 2p and (f) survey spectrum.

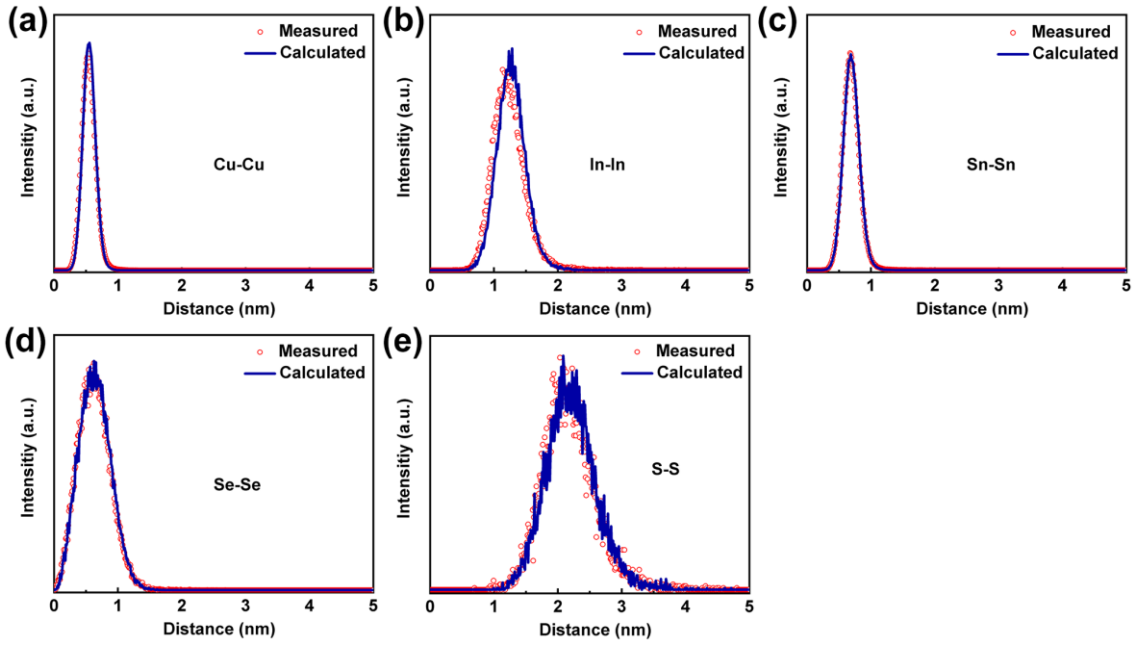

Fig. S14 Nearest-neighbor atomic distribution histograms of Cu, In, Sn, Se, S for SPSed-$Cu_2In_{0.09}Sn_{0.91}Se_2S$. The navy-blue line represents the calculated curves assuming all elements are homogeneously and randomly distributed in the material.

3. Electronic and phononic band structures

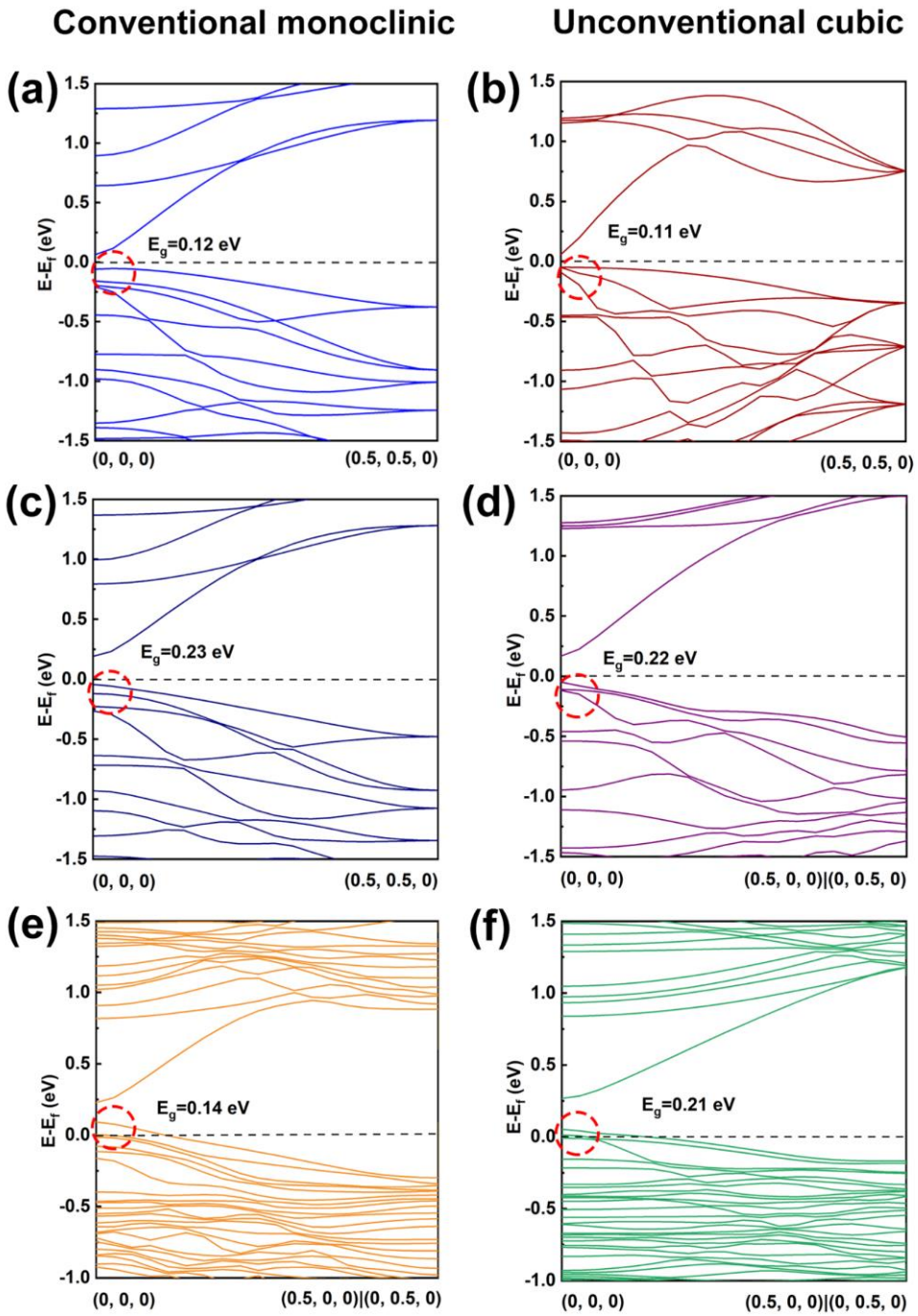

Fig. S15 The electronic energy band structures for (a) monoclinic Cu_2SnSe_3, (b) cubic Cu_2SnSe_3, (c) monoclinic Cu_2SnSe_2S, (d) cubic Cu_2SnSe_2S, (e) monoclinic $Cu_2In_{0.06}Sn_{0.94}Se_2S$ and (f) cubic $Cu_2In_{0.06}Sn_{0.94}Se_2S$.

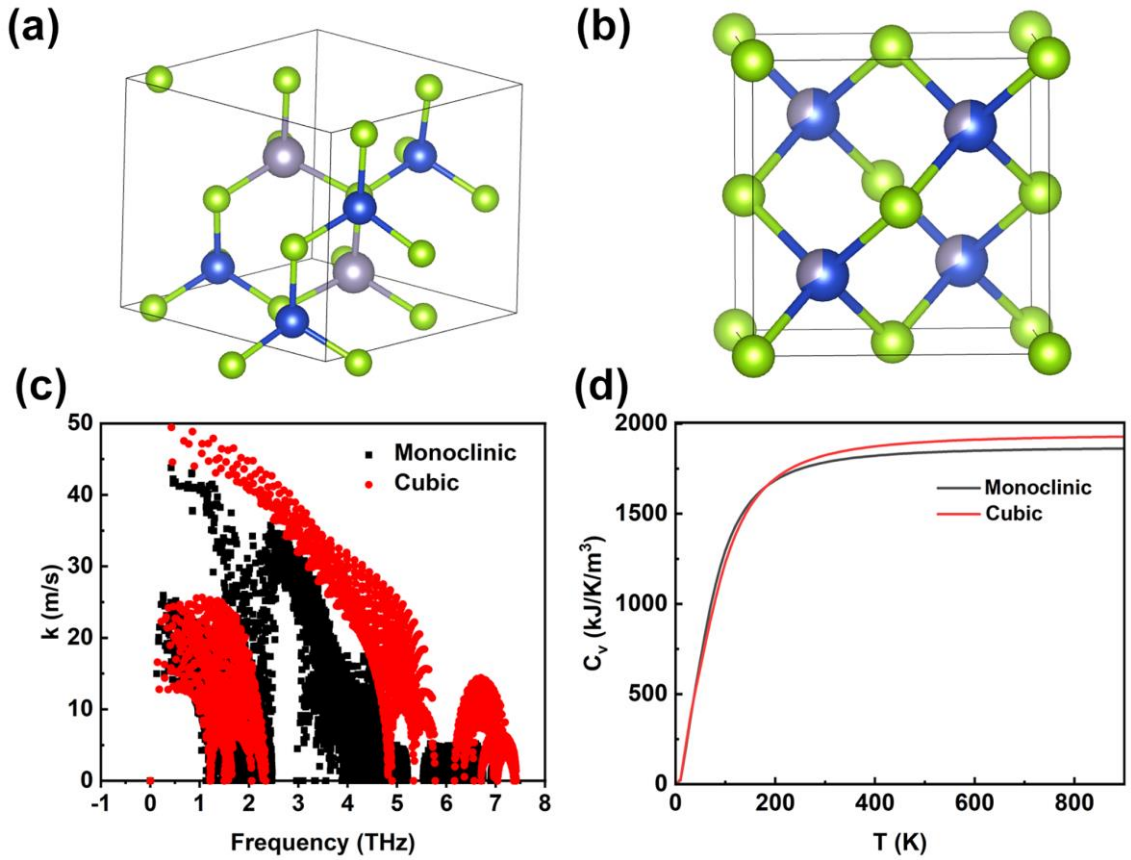

Fig. S16 The crystal structures of (a) monoclinic and (b) cubic Cu_2SnSe_3. (c) The phonon group velocity comparison and (d) the phonon heat capacity comparison between monoclinic and cubic Cu_2SnSe_3.

4. Thermoelectric properties

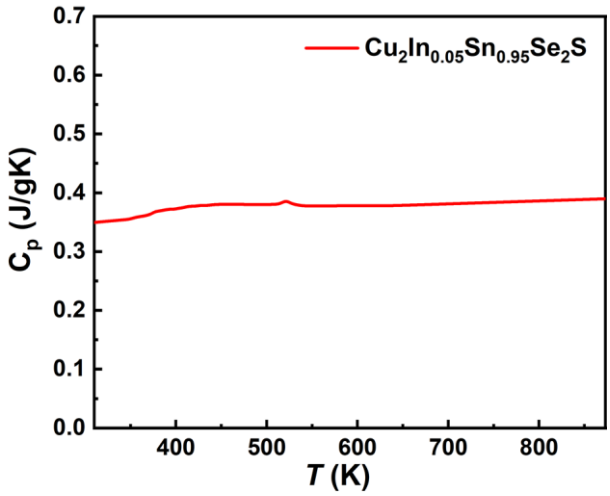

Fig. S17 Temperature dependence of specific heat capacity C_p for SPSed-$Cu_2In_{0.05}Sn_{0.95}Se_2S$.

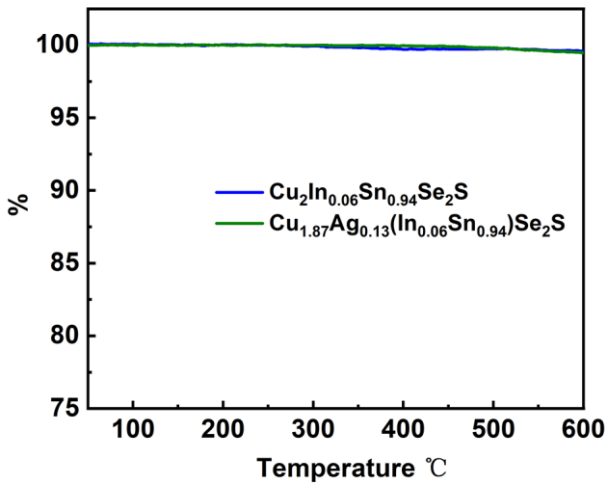

Fig. S18 Thermal gravimetric analysis (TGA) of SPSed-$Cu_2In_{0.06}Sn_{0.94}Se_2S$ and SPSed-$Cu_{1.87}Ag_{0.13}(In_{0.06}Sn_{0.94})Se_2S$ from 50 °C to 600 °C with nitrogen protection. The weight losses of both samples are less than 1%.

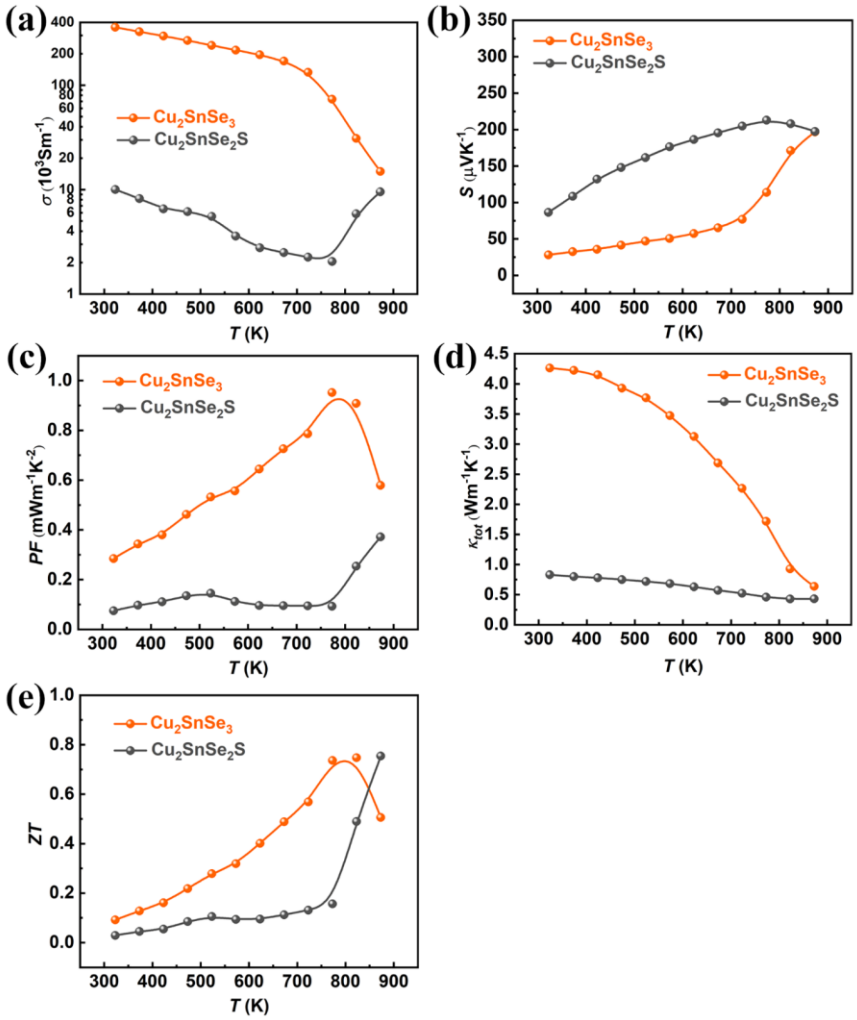

Fig. S19 Temperature dependence of (a) electrical conductivity σ; (b) Seebeck coefficient *S*, (c) power factor *PF*, (d) total thermal conductivity κ_{tot} and (e) *ZT* values for Cu_2SnSe_3 and Cu_2SnSe_2S.

Fig. S20 shows the thermoelectric properties of $Cu_2In_{0.02}Sn_{0.98}Se_2S$, $Cu_2In_{0.14}Sn_{0.86}Se_2S$, $Cu_2In_{0.4}Sn_{0.6}Se_2S$ and $Cu_3InSnSe_3S_2$ in the temperature range of 323-873 K. It is found that with a large increase of In content, the electrical conductivity σ decreases sharply (Fig. S20a) and the S value increases (Fig. S20b). Specifically, σ decreases from 7.89×10^3 S m^{-1} for $Cu_2In_{0.02}Sn_{0.98}Se_2S$ to 1.38×10^3 S m^{-1} for $Cu_3InSnSe_3S_2$ at 873 K, S increases from 225.38 μV K^{-1} for $Cu_2In_{0.02}Sn_{0.98}Se_2S$ to 288.84 μV K^{-1} for $Cu_3InSnSe_3S_2$ at 873 K. Despite the enhanced Seebeck coefficient, the power factor (PF) of $Cu_3InSnSe_3S_2$ (0.11 mW m^{-1} K^{-2} at 873 K) is smaller than that of $Cu_2In_{0.02}Sn_{0.98}Se_2S$ (0.40 mW m^{-1} K^{-2} at 873 K) (Fig. S20c) because of the lower electrical conductivity. Although the thermal conductivity decreases with the increase of In content, the ZT value of $Cu_3InSnSe_3S_2$ sample is not increased.

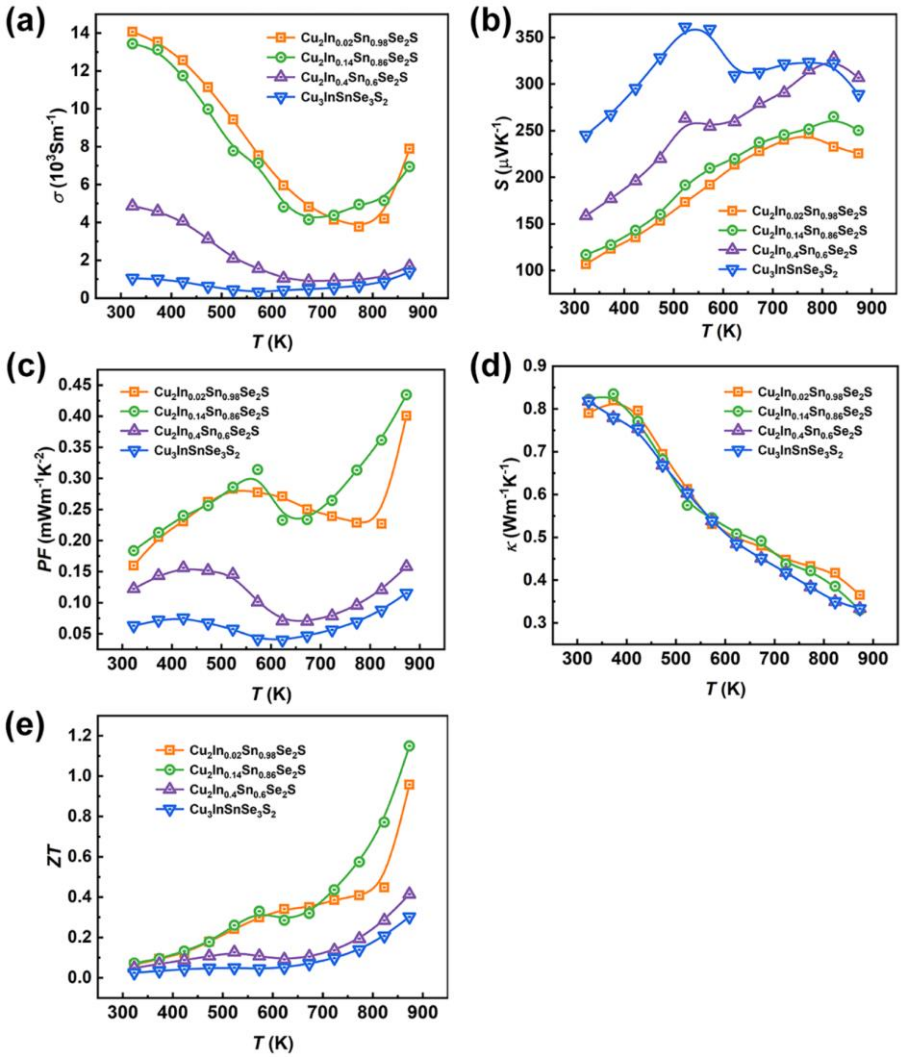

Fig. S20 Temperature dependence of (a) electrical conductivity σ; (b) Seebeck coefficient S, (c) power factor PF, (d) total thermal conductivity κ_{tot} and (e) ZT values for $Cu_2In_{0.02}Sn_{0.98}Se_2S$, $Cu_2In_{0.14}Sn_{0.86}Se_2S$, $Cu_2In_{0.4}Sn_{0.6}Se_2S$ and $Cu_3InSnSe_3S_2$.

The weighted mobility μ_w of $Cu_{2-y}Ag_y(In_xSn_{1-x})Se_2S$ (x= 0, 0.05, 0.06, 0.25, y= 0, 0.07, 0.13) was calculated from the measured electrical conductivity σ and Seebeck coefficient S according to the formula $\mu_w = 331\frac{cm^2}{V_s}\left(\frac{m\Omega\, cm}{\rho}\right)\left(\frac{T}{300\,K}\right)^{-\frac{3}{2}}\left[\frac{\exp\left[\frac{|S|}{k_B}-2\right]}{1+\exp\left[-5\left(\frac{|S|}{\frac{k_B}{e}}-1\right)\right]}+\frac{\frac{3}{\pi^2}\frac{|S|}{k_B/e}}{1+\exp\left[5\left(\frac{|S|}{\frac{k_B}{e}}-1\right)\right]}\right]$.[17] As shown in Fig. S21a, the weighted mobility of the samples is not high and decreases with temperature before 723 K because of phonon scattering. The enhancement on μ_w is especially significant near room temperature as the In doping and when the temperature reaches 773 K, the weighted mobility μ_w of $Cu_{2-y}Ag_y(In_xSn_{1-x})Se_2S$ (x= 0, 0.05, 0.06, 0.25, y= 0, 0.07, 0.13) is improved. Benefitting from the improved μ_w values, as well as the decreasing value of κ_L, the ZT value was enhanced after In-doping and Ag-alloying, which can be confirmed by the enhancement of thermoelectric quality factor B via doping In and alloying Ag (Fig. S21b). The quality factor B is designed to estimate the optimal thermoelectric performance for specified materials and proportional to the weighted mobility divided by the lattice thermal conductivity μ_w/κ_L according to the formula $B = \left(\frac{k_B}{e}\right)^2\frac{8\pi e(2m_e k_B T)^{3/2}}{3h^3}\cdot\frac{\mu_w}{k_L}T$.[17]

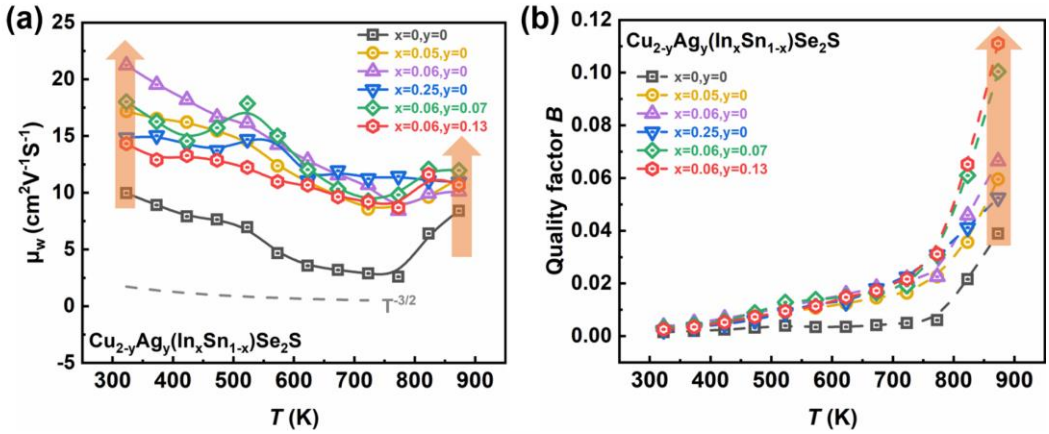

Fig. S21 (a) The weighted mobility μ_w and (b) Quality factor B as a function of temperature of $Cu_{2-y}Ag_y(In_xSn_{1-x})Se_2S$ (x= 0, 0.05, 0.06, 0.25, y= 0, 0.07, 0.13) samples.

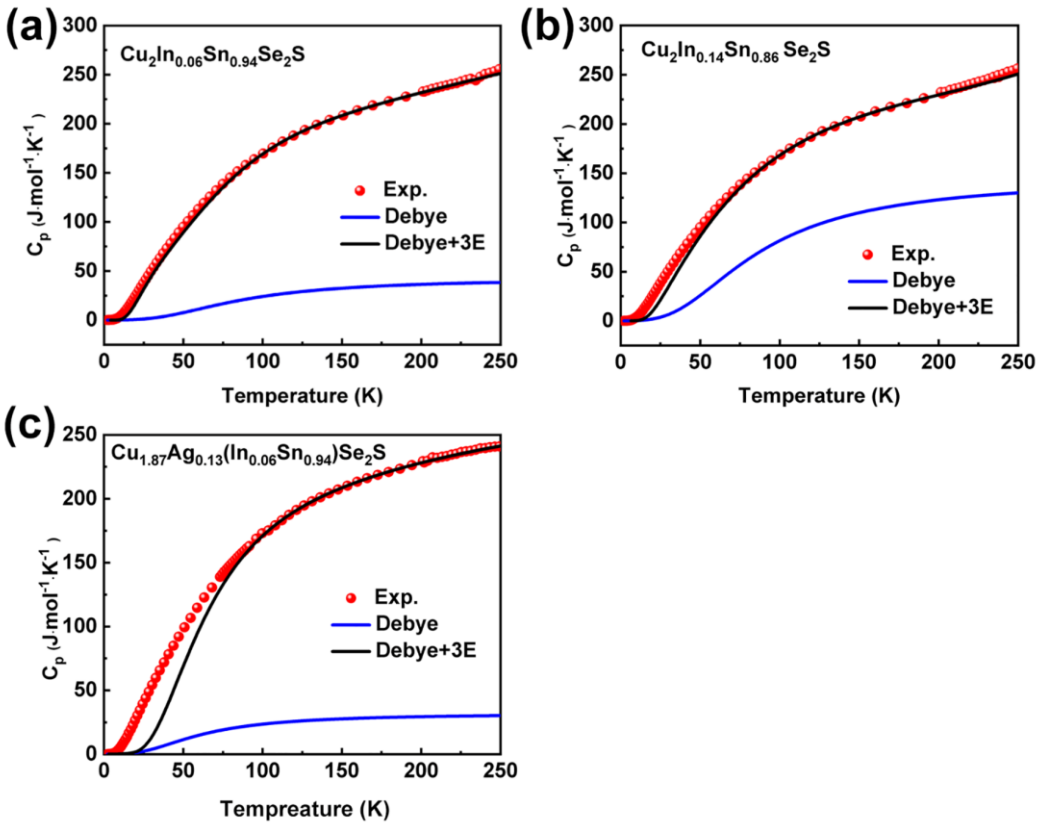

Fig. S22 The experimental C_p with respect to T at low temperature fitted by a combination of Debye and three Einstein models. Red dots illustrate the experimental heat capacity plotted as C_p versus T for (a) SPSed-$Cu_2In_{0.06}Sn_{0.94}Se_2S$, (b) SPSed-$Cu_2In_{0.14}Sn_{0.86}Se_2S$ and (c) SPSed-$Cu_{1.87}Ag_{0.13}(In_{0.06}Sn_{0.94})Se_2S$. Obviously, the data can be fitted only with the Debye–3 Einstein model rather than the Debye model.

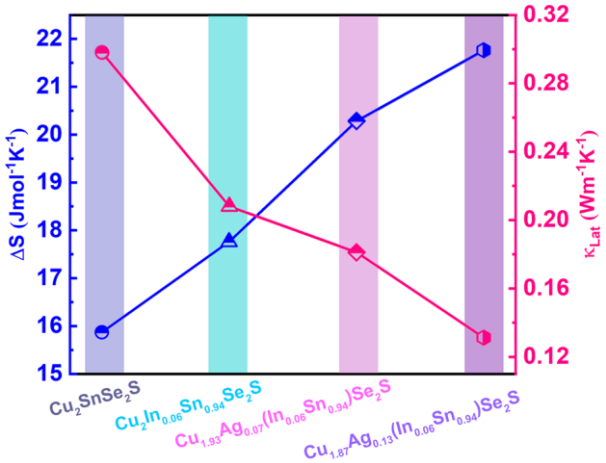

Fig. S23 Calculated configurational entropy ΔS and lattice thermal conductivities (κ_{Lat}) for Cu_2SnSe_2S, $Cu_2In_{0.06}Sn_{0.94}Se_2S$, $Cu_{1.93}Ag_{0.07}(In_{0.06}Sn_{0.94})Se_2S$ and $Cu_{1.87}Ag_{0.13}(In_{0.06}Sn_{0.94})Se_2S$.

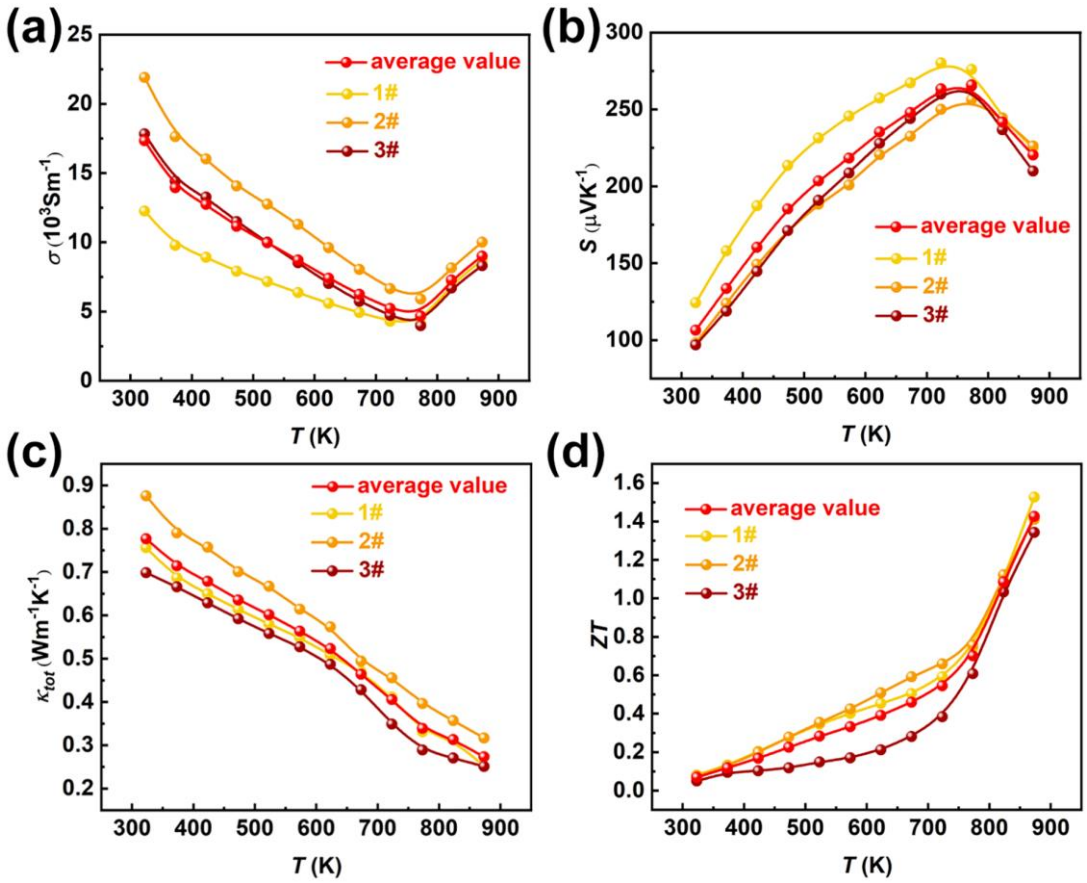

Fig. S24 Data repeatability of (a) electrical conductivity σ, (b) Seebeck coefficient *S*, (c) total thermal conductivity κ_{tot} and (d) *ZT* values for $Cu_{1.87}Ag_{0.13}(In_{0.06}Sn_{0.94})Se_2S$.

Table S4. Fitting parameters for modelling C_p vs. *T* plot given in Fig. S18 in the main text.

Parameter	
θ_{E1} (K)	305.94 K
θ_{E2} (K)	4.02 K
θ_{E3} (K)	100 K
θ_D (K)	359.19 K

Table S5. Comparison between the Present and Literature-Reported Properties of Cu_2SnSe_3-based materials.

Sample description	Synthetic strategy	Phase structure	κ_{Lat}[a] (W / mK)	μ_H[a] ($cm^2\ V^{-1}\ s^{-1}$)	(μ_H /κ_{Lat})·(m_d^*/m_e)$^{3/2}$[a] ($10^{-3}\ m^3\ KV^{-1}\ s^{-1}\ W^{-1}$)	ZT[a]
this work, $Cu_2In_{0.06}Sn_{0.94}Se_2S$	colloidal synthesis	cubic	0.68	1.75	0.21	0.07
Ming, $Cu_2Sn_{0.82}In_{0.18}Se_{2.7}S_{0.3}$[18]	melting	monoclinic	1.32	7.80	0.26	0.04
Li, $Cu_{1.85}Ag_{0.15}Sn_{0.9}In_{0.1}Se_3$[13]	ball milling	monoclinic	1.30[b]	5.23	0.17	0.06

[a] All the values are measured at ~300 K. [b] Calculated from $\kappa_{Lat} = \kappa_{tot} - \kappa_e$.

References in the supporting information

1. X. Qiu, J. W. Thompson and S. J. L. Billinge, *J. Appl. Crystallogr.*, 2004, **37**, 678.

2. C. L. Farrow, P. Juhas, J. W. Liu, D. Bryndin, E. S. Božin, J. Bloch, T. Proffen and S. J. L. Billinge, *J. Phys.: Condens. Matter.*, 2007, **19**, 335219.

3. G. Kresse and J. Furthmüller, *Phys. Rev. B.*, 1996, **54**, 11169-11186.

4. S. L. Dudarev, G. A. Botton, S. Y. Savrasov, C. J. Humphreys and A. P. Sutton, *Phys. Rev. B.*, 1998, **57**, 1505-1509.

5. A. Togo and I. Tanaka, *Scr. Mater.*, 2015, **108**, 1-5.

6. S. Kirklin, J. E. Saal, B. Meredig, A. Thompson, J. W. Doak, M. Aykol, S. Rühl and C. Wolverton, *npj Comput. Mater.*, 2015, **1**, 15010.

7. L.-D. Zhao, G. Tan, S. Hao, J. He, Y. Pei, H. Chi, H. Wang, S. Gong, H. Xu, V. P. Dravid, C. Uher, G. J. Snyder, C. Wolverton and M. G. Kanatzidis, *Science*, 2016, **351**, 141-144.

8. M. K. Jana, K. Pal, A. Warankar, P. Mandal, U. V. Waghmare and K. Biswas, *J. Am. Chem. Soc.*, 2017, **139**, 4350-4353.

9. B. Koley, A. Lakshan, P. R. Raghuvanshi, C. Singh, A. Bhattacharya and P. P. Jana, *Angew. Chem. Int. Ed.*, 2021, **60**, 9106-9113.

10. J. L. Baker, J. T. White, A. Chen, T. Ulrich, R. R. Roback and H. Xu, *J. Nucl. Mater.*, 2021, **557**, 153282.

11. Y. Lou, W. Zhao, C. Li, H. Huang, T. Bai, C. Chen, C. Liang, Z. Shi, D. Zhang, X.-B. Chen and S. Feng, *ACS Appl. Mater. Interfaces.*, 2017, **9**, 18046-18053.

12. Y. Cui, G. Wang and D. Pan, *CrystEngComm*, 2013, **15**, 10459-10463.

13. Y. Li, G. Liu, T. Cao, L. Liu, J. Li, K. Chen, L. Li, Y. Han and M. Zhou, *Adv. Funct. Mater.*, 2016, **26**, 6025-6032.

14. H. Zhang, T. Ouyang, J. Li, M. Mu and X. Yin, *Electrochim. Acta.*, 2021, **390**, 138766.

15. L. Tan, Z.-Q. Liu, N. Li, J.-Y. Zhang, L. Zhang and S. Chen, *Electrochim. Acta*., 2016, **213**, 283-290.
16. C.-T. Yang, H.-I. Hsiang and J.-H. Tu, *Adv. Powder Technol.*, 2016, **27**, 959-963.
17. G. J. Snyder, A. H. Snyder, M. Wood, R. Gurunathan, B. H. Snyder and C. Niu, *Adv. Mater.*, 2020, **32**, 2001537.
18. H. Ming, G. Zhu, C. Zhu, X. Qin, T. Chen, J. Zhang, D. Li, H. Xin and B. Jabar, *ACS Nano*, 2021, **15**, 10532-10541.